RSC Applied Interfaces

ROYAL SOCIETY OF CHEMISTRY

REVIEW

View Article Online
View Journal | View Issue

Cite this: *RSC Appl. Interfaces*, 2025, **2**, 1537

Decoding mass transport in electrochemical systems *via in situ* laser interferometry

Junshuo Lian,[a] Zhongxi Zhao,*[a] Jianwen Yu,[a] Jiangfeng Huang,[a] Yaoming Leng[a] and Peng Tan *[ab]

Received 25th July 2025,
Accepted 9th September 2025

DOI: 10.1039/d5lf00212e

rsc.li/RSCApplInter

Probing ion transport dynamics at electrode–electrolyte interfaces is essential for advancing electrochemical energy technologies. Among various diagnostic methods, laser interferometry stands out as a label-free, non-invasive optical technique with high spatiotemporal resolution, which is uniquely suited for *in situ* visualization of interfacial concentration fields. This work outlines the fundamental optical principles and system configurations of laser interferometry, including Mach–Zehnder interferometers and digital holography. Key data processing strategies for concentration field reconstruction are presented, including fringe shift analysis, phase-shifting interferometry, and digital holography. Representative applications are discussed, with a focus on interfacial concentration evolution, metal electrodeposition and dendrite growth, and mass transport under magnetic or convective effects. By bridging optical interferometry with electrochemical interface science, this work provides a comprehensive methodological framework and offers practical guidance for researchers exploring mass transport phenomena and optimizing the performance of electrochemical systems.

1. Introduction

The ion concentration field at the electrode–electrolyte interface plays a pivotal role in governing the performance of electrochemical systems. Accurate characterization of its spatial distribution and temporal evolution is essential for unveiling the coupling mechanisms between interfacial mass transport and overall electrochemical behaviors, thereby deepening the understanding of underlying physicochemical processes. Although numerous mathematical models have been developed to describe ion migration and concentration profiles in such systems, they are typically based on a series of idealized assumptions.[1,2] Consequently, considering the complex realities of practical systems, such as electrode reaction inhomogeneity, nonuniform initial electrolyte conditions, natural or electroconvective flows and structural heterogeneity within the cell, these discrepancies significantly limit the predictive reliability of such systems under real-world operating conditions.[3] This underscores the urgent need for intuitive, accurate, and *in situ* observation techniques that are capable of directly visualizing ion transport at electrochemical interfaces, thereby enabling model refinement, device optimization, and performance enhancement.

To address this challenge, various *in situ* imaging techniques based on physical field responses have been developed. Representative examples include *in situ* Raman spectroscopy,[4–8] nuclear magnetic resonance imaging (NMR),[9–12] *in situ* fluorescence microscopy,[13–16] and scanning ion conductance microscopy (SICM).[17] For example, Klett *et al.* employed *in situ* ^{7}Li NMR imaging to visualize the evolution of lithium-ion concentration gradients in an electrolyte.[12] Takahashi *et al.* utilized SICM to reveal the correlation between the local ion distribution and nanoscale electrode surface morphology.[17] Chen *et al.* visualized real-time two-dimensional pH distributions at the electrode–electrolyte interface of a zinc–air battery *via* laser scanning confocal microscopy (LSCM).[14] Despite their respective advantages, each of these techniques presents inherent limitations: Raman spectroscopy is restricted to species possessing Raman-active functional groups; NMR instruments are costly and offer limited temporal resolution owing to long acquisition times; fluorescence microscopy often requires exogenous fluorescent probes, which may induce quenching effects or chemical interference; and SICMs operate in close proximity to the sample, posing risks of mechanical disturbance, while point-by-point scanning inherently limits imaging speed. As summarized in Table 1, a comparative framework was established by integrating quantitative parameters, representative application scenarios, and associated limitations. This framework highlights the unique advantages

[a] *Department of Thermal Science and Energy Engineering, University of Science and Technology of China (USTC), Hefei 230026, Anhui, China.*
E-mail: zzx98@ustc.edu.cn, pengtan@ustc.edu.cn
[b] *State Key Laboratory of Fire Science, University of Science and Technology of China (USTC), Hefei 230026, Anhui, China*

Table 1 Performance comparison of different *in situ* imaging techniques for electrochemical interface studies

Technique	Lateral spatial & temporal resolution	Detection limit	Representative applications	Limitations	Ref.
Laser interferometry/ digital holography	0.3–10 μm; 0.01–0.1 s (up to 10^{-6}–10^{-4} s with high-speed cameras)	$<10^{-4}$ mol L^{-1} concentration change	Real-time full-field monitoring of refractive index (concentration) fields near electrodes	Requires transparent optical windows; measures overall changes without species specificity; sensitive to vibration and temperature	18
Nuclear magnetic resonance imaging (NMR)	50–500 μm; seconds–minutes (fast MRI: 20–30 ms)	10^{-5}–10^{-3} mol L^{-1}, depending on nucleus and sample volume	3D mapping of species distribution, dendrite growth, or corrosion; chemical selectivity	Low spatiotemporal resolution; expensive instrumentation; unsuitable for paramagnetic materials	19
Raman spectroscopy imaging	0.3–10 μm; 0.5–60 s per spectrum at a single point; minutes–hours for mapping	$\sim10^{-6}$ mol L^{-1} (non-resonant Raman)	Molecular fingerprinting; identification of specific species and crystalline phases	Weak signals requiring accumulation; poor temporal resolution; prone to fluorescence interference	20
Fluorescence imaging (laser scanning confocal microscopy, LSCM)	0.2–1 μm; 0.01–0.1 s (limited by camera frame rate)	10^{-7}–10^{-6} mol L^{-1}, probe-dependent	Quantification of specific ion concentrations with fluorescent probes; 2D/3D imaging	Requires exogenous probes, which may perturb the system; photobleaching and phototoxicity effects	21
Scanning ion conductance microscopy (SICM)	10–20 nm; seconds–minutes (high-speed SICM: 0.5–20 s per frame)	Down to single molecule level, probe- and system-dependent	Surface morphology, local ion concentration, and surface charge mapping at electrodes	Slow scanning and limited field of view; measurements affected by convection; complex and expensive instrumentation; probe may disturb the local environment	22

of laser interferometry in terms of spatiotemporal resolution, non-invasiveness, and full-field dynamic imaging. Therefore, the development of *in situ* imaging technologies that simultaneously offer high spatial resolution, non-invasiveness and fast temporal responsiveness remains a critical challenge in the field of electrochemical interface characterization.

In this context, laser interferometric techniques have emerged as promising candidates for *in situ* visualization of ion transport behavior at electrochemical interfaces. These techniques are particularly attractive due to their label-free, non-contact, and non-invasive nature, along with their submicron spatial resolution and excellent temporal responsiveness. By detecting changes in the refractive index of the electrolyte caused by ion concentration gradients, laser interferometry captures the resulting optical path length differences and reconstructs phase distributions. This enables high-resolution imaging of critical interfacial processes such as the development of concentration gradients, ion depletion phenomena, and diffusion layer formation.

The application of laser interferometry to electrochemical systems dates back to the 1960s. As early as 1967, researchers began employing interferometric methods to observe diffusion boundary layers at electrode interfaces, establishing a foundation for their use in electrochemical interfacial studies.[23] Since then, the technique has been widely employed in corrosion, electrodeposition, and related fields to investigate interfacial mass transport and concentration field evolution under both aqueous and non-aqueous conditions.[24–33] With the advent of high-performance charge-coupled device (CCD)/ complementary metal-oxide semiconductor (CMOS) sensors and advances in digital image processing algorithms, the 21st century witnessed the maturation of digital holography based on interferometric principles.[34–42] These developments have significantly enhanced spatiotemporal resolution, enabling precise dynamic analyses of interfacial concentration fields and reaction kinetics in systems such as metal corrosion and electrodeposition. More recently, the advantages of laser interferometry, particularly its non-invasiveness and high sensitivity, have been harnessed in the study of battery interface phenomena. Applications in lithium-ion, aqueous, and lithium-sulfur battery systems have demonstrated their unique ability to capture complex interfacial processes dynamically, positioning laser interferometry as an increasingly important tool in the study of electrochemical interfaces.

In this work, the fundamental principles, representative applications, and future development directions of laser interferometry in the context of interfacial concentration field research are systematically reviewed. First, the fundamental optical principles and typical configurations of laser interferometry are introduced, and its advantages and limitations in electrochemical applications are evaluated. Then, major quantitative analysis methods, such as fringe shift analysis, phase-shifting interferometry, and digital holography, are summarized, with a focus on their capabilities in reconstructing ion concentration fields with high spatial and temporal resolution. Furthermore, representative applications are categorized based on distinct interfacial transport phenomena, including concentration gradient development, metal deposition and dendrite growth, and mass transport under external fields such as magnetic modulation or electroconvection. Finally, recent advances in multimodal integration and intelligent data processing are highlighted, and

current challenges and future opportunities for laser interferometry in electrochemical interface analysis are discussed. Through this work, a methodological reference and a technical foundation are established to support future research on interfacial mass transfer and mechanistic exploration in next-generation electrochemical systems.

2. Principle of laser interferometry

2.1. Optical principle of laser interferometric measurement

Laser interferometry enables non-invasive visualization of the dynamic evolution of concentration fields at electrode interfaces by capturing time-dependent changes in the coherent superposition of the object beam and reference beam on the detector plane. This work specifically focuses on *in situ* applications of laser interferometry in electrochemical systems, where it is primarily employed to characterize mass transport behaviors at the electrode–electrolyte interface.[43–50] Key applications include the extraction of diffusion coefficients, tracking of concentration distributions, and analysis of the effects of convection on interfacial mass transfer. In particular, this review focuses on lateral interferometry, a configuration in which the laser beam illuminates the electrode-electrolyte interface from the side, *i.e.*, at an oblique angle rather than vertically. This geometry, as shown in Fig. 1(a), is particularly suitable for visualizing ion concentration gradients parallel to the electrode surface. This scope explicitly excludes surface metrology applications, such as nanometer-scale displacement detection and thin film thickness measurement, which typically involve a near-normal incident geometry, as shown in Fig. 1(b).[51–53]

With respect to system geometry, Fig. 1(c) presents a typical vertical configuration, where the electrode is oriented along the gravitational direction (negative y-axis in the figure), a setup that often easily induces natural convection. In contrast, when the system is rotated 90° clockwise about the z-axis such that the original x-axis becomes vertically downwards, it corresponds to a horizontal configuration, as illustrated by the electrochemical cell layout in Fig. 1(d).

The core principle of laser interferometry lies in monitoring the phase difference $\Delta\phi$ between the object and reference beams, as it varies with the physical parameters of the system (*e.g.*, concentration, temperature and thickness). This variation alters the observed interference pattern, thereby enabling dynamic and non-contact visualization of interfacial phenomena. The intensity distribution I on the detector is given by:[55]

$$I = I_O + I_R + 2\sqrt{I_O I_R}\cos(\Delta\phi) \quad (1)$$

where I_O and I_R are the intensities of the object beam and reference beam, respectively, and where $\Delta\phi$ is the phase difference between them. This phase difference can be further decomposed into a spatially varying component $\Delta\phi_1$ and a constant offset $\Delta\phi_0$. Through spatial mapping, the interference pattern recorded on the detector can be projected back onto the Oxy plane of the sample shown in Fig. 1(c), thus enabling the reconstruction of two-dimensional behaviors at the electrode–electrolyte interface.

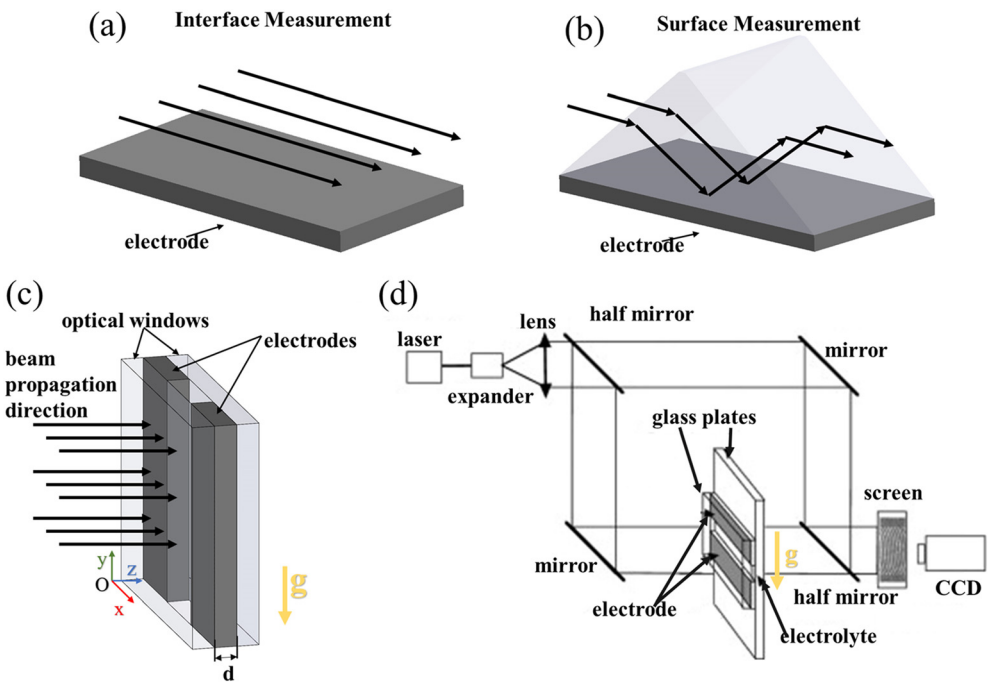

Fig. 1 Schematic configurations of laser interferometry systems for electrochemical interface measurements. Schematic diagram of the optical path for laser interferometry at the (a) interface and (b) surface. (c) Schematic illustration of the electrochemical cell configuration used for interferometric measurements. (d) Basic optical path layout of the Mach–Zehnder interferometer.[54] Adapted from ref. 54 with permission from Elsevier, copyright.

In electrochemical studies where the primary interest lies in optical path length variations induced by refractive index changes within the electrolyte, $\Delta\phi$ can be expressed as:

$$\Delta\phi = (2\pi/\lambda)\Delta L = (2\pi/\lambda)\Delta n{\cdot}d \quad (2)$$

where λ is the laser wavelength, $\Delta n = (\bar{n} - n_0)$ represents the average change in the refractive index along the laser propagation direction (z-axis in Fig. 1(c)), and d is the beam path length through the electrolyte.

Furthermore, assuming that the refractive index change of the solution is caused solely by changes in the solution concentration, the concentration–refractive index relationship can be expressed as:

$$n = f(c) \quad (3)$$

where c is the molar concentration of the electrolyte. In many electrolyte systems, the refractive index n and concentration c are approximately linearly related. For example, in a $ZnSO_4$ solution at 20 °C under He–Ne laser illumination, the fitting relationship $n = 1.3313 + 0.0232c$ with c in mol L^{-1}.[30] This linearity enables direct mapping of interference fringe evolution to spatial variations in concentration, allowing *in situ* visualization of diffusion layer growth and concentration gradient dynamics.

On this basis, the Mach–Zehnder interferometer, with its open and flexible optical architecture, provides an ideal platform for interface measurements. Its sample arm can be readily integrated with custom-designed electrochemical cells for investigating localized ion concentration changes, the formation of diffusion layers, and associated mass transport phenomena.

Fig. 1(d) illustrates the standard optical layout of the Mach–Zehnder interferometer. A collimated laser beam is divided into object and reference paths at the first beam splitter. The object beam passes through the electrochemical cell, where it interacts with the sample and encodes spatial variations in the refractive index, whereas the reference beam travels through a stable air path. The two beams are subsequently recombined at the second beam splitter to generate an interference pattern on the detector.[28] During electrochemical reactions, the evolving ion distribution near the electrode interface continuously modifies the local refractive index field within the electrolyte. These changes dynamically alter the optical path length of the object beam, leading to a corresponding modulation in the $\Delta\phi$ between the object and reference beams. As a result, the interference fringes undergo observable shifts in both position and morphology. By analysing fringe changes, one can reconstruct interfacial mass transport processes either semi-quantitative or fully quantitatively. The parameters that can be extracted include concentration gradients at the electrode–electrolyte interface, the temporal evolution of the diffusion layer thickness, and the onset or development of localized convection. Owing to its non-invasive nature, high sensitivity, and submicron spatial resolution, Mach–Zehnder interferometry provides a powerful tool for real-time visualization and mechanistic investigation of electrochemical interface dynamics.

2.2. Quantitative reconstruction and concentration field analysis from interferograms

Fringe image analysis in interferometric measurements typically falls into four categories. The fundamental principles of each approach are outlined below.

Qualitative analysis (correlation between fringe density and concentration gradient). In interference imaging, the phase difference between adjacent bright or dark fringes corresponds to 2π. Consequently, fringe density can be interpreted as a spatial representation of the local phase gradient. According to eqn (2) and (3), regions with higher fringe density correspond to larger refractive index gradients and thus steeper concentration gradients, whereas sparsely fringed regions reflect gentler concentration variations. As shown in Fig. 2(a), region B results in denser fringes than does region A, indicating a stronger local concentration gradient.

Quantitative analysis of fringe shift. Expanding upon qualitative analysis, the concept of fringe shift number S is introduced, defined as the number of full fringe displacements (of the same type bright-to-bright or dark-to-dark) at a given spatial point relative to the initial reference state. The resulting phase shift at this point is $\Delta\phi = 2\pi S$. For example, at the reference point highlighted in Fig. 2(b–e), $S = 4$; thus, $\Delta\phi = 8\pi$. By substituting eqn (2), a direct relationship between S and the average refractive index change Δn can be derived:

$$\Delta n = \frac{S{\cdot}\lambda}{d} \quad (4)$$

This expression provides a straightforward mathematical basis for reconstructing the concentration field. By measuring S at selected reference points in the interference image and using known values for d and λ, the corresponding Δn can be calculated. With a known refractive index-concentration calibration (*e.g.*, eqn (3)), this enables pointwise quantitative reconstruction of the spatial concentration distribution.

Quantitative analysis *via* isoconcentration line approximation. This method can be considered an extension of the phase-shift interferometry, a technique originally proposed by Watt and Vest and widely applied in the inversion of refractive index distributions in fluid flow, thermal fields, and optical systems.[58] Its typical optical path configuration is illustrated in Fig. 2(f). Compared with the basic Mach–Zehnder setup in Fig. 1(d), a key modification is the introduction of a piezoelectric transducer (PZT)-controlled mirror (M1) in the reference beam path, allowing high-precision modulation of the optical phase.

In practice, the PZT is used to precisely control the constant term $\Delta\phi_0$ in $\Delta\phi$, enabling the acquisition of a series of phase-shifted interference images. In the four-step phase-shift method, $\Delta\phi_0$ is sequentially set to 0, $\pi/2$, π and $3\pi/2$, resulting in four intensity frames I_1, I_2, I_3 and I_4. These are

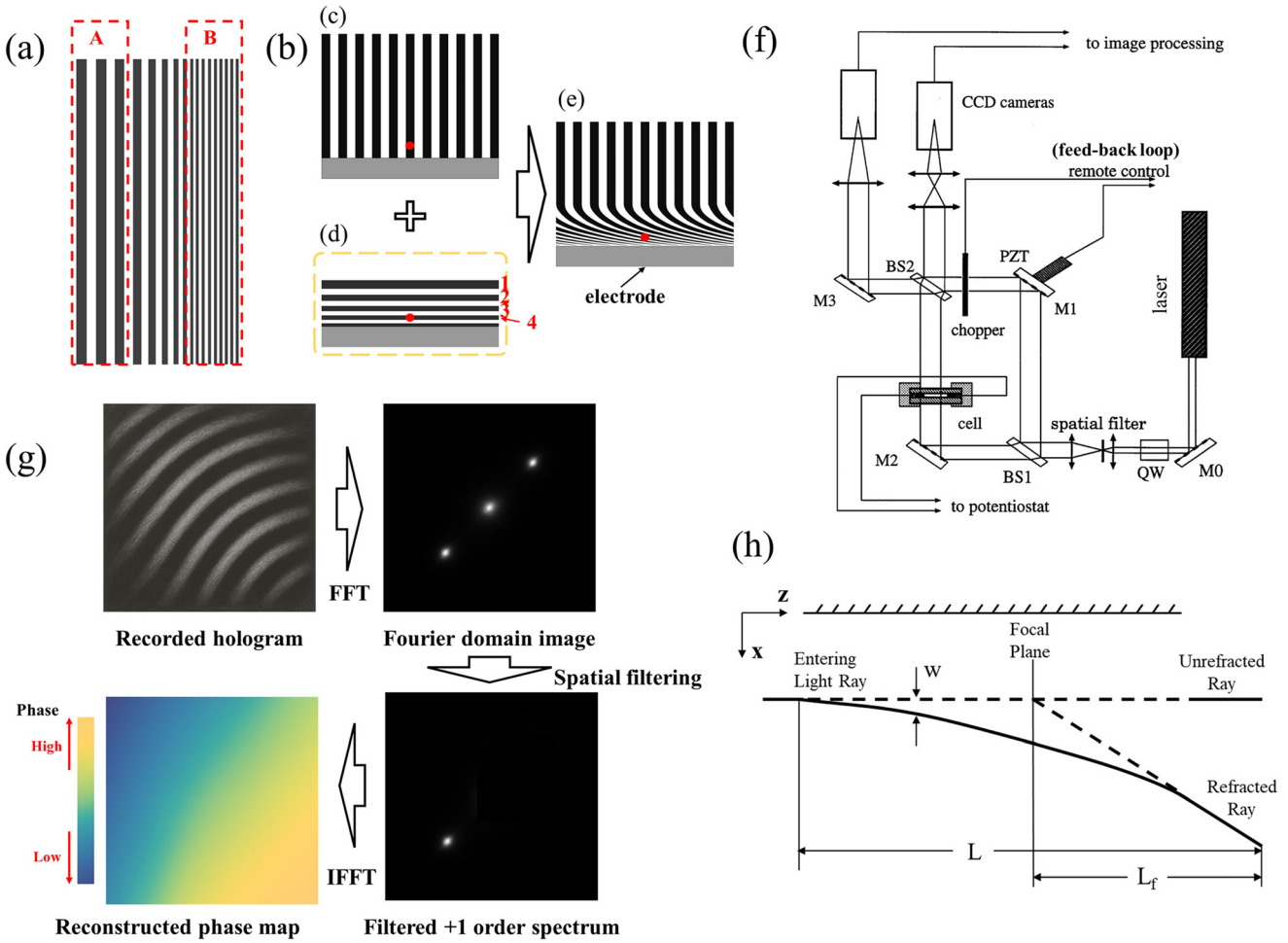

Fig. 2 Schematic diagram of the principle for reconstruction in interferometric visualization of concentration fields. (a) Qualitative correlation between fringe density and concentration gradient. (b–e) Principle of fringe shift analysis: (c) initial reference fringes, (d) fringe distribution induced by the concentration field at the electrode surface (dashed box represents hypothetical diagram), (e) actual observed fringe image as the superposition of (c) and (d), with a red dot indicating the selected spatial reference point. (f) Mach–Zehnder interferometer with integrated feedback control.[56] Reproduced from ref. 56. With permission from the American Physical Society, copyright. (g) Schematic diagram illustrating the principle of digital holography. (h) Schematic diagram of a refracted ray. Here, w denotes the deflection angle of the refracted ray, L is the length of the test section, and L_f is the distance between the focal plane and the exit plane.

then combined to compute the local phase distribution *via* the following expression:

$$\phi = \tan^{-1}\left(\frac{I_2 - I_4}{I_3 - I_1}\right) \quad (5)$$

This approach offers high accuracy in two-dimensional phase reconstruction. However, it requires sequential frame acquisition, which limits its applicability for studying fast transient processes. Therefore, it is best suited for systems with relatively slow concentration evolution or those approaching steady-state conditions.

To address this limitation, a modified Mach–Zehnder interferometric scheme has been developed. Prior to initiating the electrochemical reaction, a feedback loop is employed to drive the PZT and adjust the reference beam such that destructive interference with the object beam occurs. This sets the system to a near-zero-fringe state, effectively resulting in an infinite fringe spacing. Once the reaction begins, concentration-induced changes in the refractive index regenerate interference fringes. Under these conditions, the newly formed fringes can be approximately treated as isoconcentration contours. Based on this approximation and combining eqn (2)–(4), the concentration difference Δc between two adjacent similar fringes can be expressed as:

$$\Delta c = f^{-1}(\lambda/d) \quad (6)$$

where $f^{-1}(\cdot)$ denotes the inverse of the refractive index-concentration calibration $n = f(c)$. In practical applications, the midpoint between adjacent fringes is often used as the representative location for evaluating concentration. Other points can then be reconstructed through interpolation. For example, in the aforementioned zinc sulfate system, with a known relationship of $n = 1.3313 + 0.0232c$, the concentration difference between adjacent similar fringes is calculated as $\Delta c = \lambda/0.0232d$ mol L^{-1}.

Quantitative reconstruction of concentration field *via* digital holography. The fringe analysis methods discussed above largely depend on manual identification, which imposes limitations in terms of processing precision and automation. In contrast, digital holography (DH) enables simultaneous extraction of both the amplitude and phase information of the optical field from a single-frame interference image. This allows for high-precision, full-field, and automated reconstruction of the phase distribution across the observed region, significantly improving both the accuracy and efficiency of concentration field visualization.[59]

With the advent of charge-coupled device (CCD)/complementary metal-oxide semiconductor (CMOS) image sensors and advances in computational optics, optical interferometry has gradually transitioned to digital techniques. In 1994, Schnars and Jüptner acquired interference images *via* a CCD and performed diffraction reconstruction in the numerical domain, marking the official advent of DH.[60] DH can be classified into transmission-type and reflection-type modalities based on the light propagation geometry.[59,61,62] Among these methods, transmission-type digital holographic interface imaging (DHII), typically implemented *via* Mach–Zehnder interferometer, is widely used for *in situ* electrochemical interface visualization and is the focal DH variant discussed in this review.

During the DH recording process, let O and R denote the complex amplitudes of the object and reference beams, respectively. The recorded interference intensity I on the detector is expressed as:

$$I(x, y) = |O(x, y)|^2 + |R(x, y)|^2 + O(x, y)R^*(x, y) + O^*(x, y)R(x, y) \quad (7)$$

where O* and R* are the complex conjugates of the object and reference beams, respectively. Here, the first two terms $|O|^2$ and $|R|^2$ represent the zero-order (background) wavefronts of the object and reference beams. The third term OR*, referred to as the +1-order wave, carries all the essential wavefront information of the object beam and is required for accurate reconstruction. The fourth term O* R corresponds to the −1-order wave and represents the conjugate wavefront.

In the numerical reconstruction phase (illustrated in Fig. 2(g)), the recorded interference pattern undergoes a Fourier transform to yield the spatial frequency domain. A filtering operation is then applied to isolate the +1-order wave by removing the zero-order and −1-order components. An inverse Fourier transform is finally performed on the filtered component to reconstruct the complex amplitude and extract the phase distribution of the object wave. By combining this result with eqn (2)–(4), the reconstructed phase distribution can be translated into a two-dimensional concentration field.

DHs offer several key advantages: single-frame acquisition, full-field measurement, high automation, and strong robustness to experimental noise. These attributes make it a mainstream method for balancing accuracy and computational efficiency in modern concentration field imaging. Although DH significantly improves the reconstruction fidelity in optical phase imaging, it should be noted that, as with the aforementioned three fringe image analysis methods, in electrochemical studies, the recovered concentration distribution usually represents an optical path-integrated (*i.e.*, projected) field. In other words, the extracted refractive index change is averaged along the laser propagation direction (z-axis in Fig. 1(c)) and thus corresponds to a two-dimensional projection rather than a volumetric distribution. While DH theoretically allows for 3D wavefront recovery and tomographic reconstruction *via* multi-angle acquisition, its current applications in electrochemical research remain largely confined to two-dimensional phase mapping. There are two primary reasons for this limitation. First, achieving 3D or specific cross-sectional concentration field reconstructions would require multi-beam interference structures, high-frame-rate image capture, and complex numerical reconstruction algorithms, greatly increasing both experimental and computational burdens. Second, in most electrochemical systems, interfacial concentration changes are predominantly confined to the direction normal to the electrode surface. As such, 2D concentration mapping on the Oxy plane is generally sufficient for resolving key interfacial mass transport phenomena, including diffusion, convection, and ion depletion.

In summary, although DH has a greater information dimension and reconstruction potential than traditional optical interferometry does, it is still mainly used for two-dimensional projection concentration fields in electrochemical applications. Its key value lies in providing high-resolution, high-frequency imaging capabilities for interface studies, enabling more precise and automated analysis of phenomena such as diffusion layer development and interfacial disturbance responses. DH can thus be considered a digital-era extension and enhancement of classical optical interferometric techniques.

2.3. Spatiotemporal suitability and quantitative reliability of interferometric techniques for electrochemical interfaces

The applicability and feasibility of interferometric techniques for monitoring concentration fields at electrochemical interfaces can be systematically evaluated by aligning their resolution capabilities with the characteristic spatial and temporal scales of interfacial mass transport processes. In diffusion-controlled electrochemical systems, the diffusion layer thickness δ can be estimated from limiting current conditions and typically falls within the range of several hundred micrometres or even greater.[63–65] Even under conditions approaching turbulent flow, δ generally remains on the order of tens of micrometres. In most standard electrochemical experiments, particularly those involving natural convection or low-disturbance environments, diffusion layers commonly exceed 100 μm.[64,66–68] The temporal evolution of concentration profiles can be characterized *via* the classical diffusion scaling relation $\delta \sim \sqrt{Dt}$. For a representative diffusion coefficient of $D \sim 10^{-5}$ cm^2 s^{-1}, a diffusion distance of ~100 μm corresponds to a timescale ranging from several seconds to minutes.[66] Hence,

dynamic changes in the interfacial concentration field typically unfold over time windows of seconds to several minutes.

In alignment with the characteristic scales of electrochemical interface processes, current laser interferometric platforms demonstrate high-resolution capabilities in both spatial and temporal dimensions. The lateral spatial resolution of an interferometric system is governed primarily by the laser wavelength, the optical magnification of the imaging setup, the pixel size of the detector, and the distance between the sample and the imaging plane.[69,70] Modern commercial digital holographic microscopes (such as those in the Lyncee Tec series) can achieve micron or submicron resolution on the Oxy observation plane, down to ~0.5 μm. This approach is sufficient to resolve critical features such as diffusion layer evolution and localized concentration fluctuations in most electrochemical scenarios. The temporal resolution is mainly limited by the frame rate of the imaging sensor and the stability of the light source. Common high-speed CCD/CMOS detectors now routinely enable acquisition intervals as short as 10 ms or less, which meets the demands for capturing rapid interfacial events such as transient current responses, gas bubble dynamics, and electroconvective perturbations.

Taken together, these considerations indicate that in typical electrochemical systems, the evolution of the interfacial concentration field generally occurs over spatial scales greater than 100 μm and on timescales ranging from seconds to minutes. Laser interferometric imaging technology, with its micron- to submicron-level spatial resolution and millisecond temporal responsiveness, enables non-invasive and *in situ* acquisition and analysis of such fields, fully satisfying the fundamental spatiotemporal requirements for characterizing interfacial mass transport.

Merely achieving sufficient spatiotemporal resolution is not adequate to support model-level inferences. To ensure that interferometric measurements can be reliably used to validate and refine mass transport theories, quantitative reliability must also be established. The following summarizes the major sources of error in interferometric measurements and corresponding calibration strategies:

(1) Beam deflection and thickness averaging. When no refractive index gradient exists along the beam propagation direction (z-axis in Fig. 1(c)), the emergent beam is not deflected, and no refraction error occurs. However, once a gradient is present, the probing beam deviates from its original path, leading to pseudo-fringe shifts in the interferogram, as illustrated in Fig. 2(h). Relevant analyses can be found in the work of Mehta and Worek.[57] To mitigate such errors, strategies include shortening the optical path, employing longer-wavelength light sources, optimizing the incidence angle and focal plane position, and applying correction algorithms based on experimentally calibrated refractive index-concentration relations.[57,71–74]

(2) Temperature coupling. Temperature perturbations in the solution are likewise encoded into phase variations, especially when reaction heat effects or Joule heating cannot be neglected. Common decoupling strategies include using independent thermometric measurements to subtract thermal contributions during data analysis, or employing dual-wavelength interferometry to establish two equations based on dispersion properties, thereby separating temperature and concentration fields.[75–78]

(3) Noise. Environmental disturbances (pressure fluctuations, temperature drift, and mechanical vibration) often introduce low-frequency phase noise, manifested as unstable background fringes. Optical noise sources (*e.g.*, laser phase noise, thermal noise in optical elements) reduce fringe contrast in long-term measurements. Detector readout noise and dark current noise further degrade the signal-to-noise ratio, particularly under low illumination or steep gradients. Typical countermeasures include vibration isolation and thermal stabilization, low-noise frequency-stabilized lasers, thermally stable optical paths, and high-sensitivity detectors combined with numerical denoising algorithms.[79–81]

(4) Nonlinearity of the refractive index–concentration relation. At low concentrations, refractive index can often be approximated as a linear function of concentration. However, this assumption breaks down in the medium-to-high concentration range, where experimental calibration and the use of piecewise or more complex fitting functions become necessary.

(5) Algorithms and numerical processing. Systematic errors may arise from phase unwrapping and Fourier-domain filtering, particularly near boundaries, as well as from improper masking. The choice and implementation details of phase unwrapping and filtering algorithms directly determine reconstruction quality. Recently, combined approaches such as quality-guided spatial unwrapping with window-function Fourier filtering have been widely adopted. More notably, advances in machine learning and deep neural networks are enabling automated fringe recognition, phase unwrapping, and error suppression, offering superior performance in phase retrieval from complex interferograms.[82–85]

As a result, this technique exhibits excellent adaptability and experimental versatility in applications such as concentration distribution mapping, diffusion layer structure reconstruction, transient disturbance tracking, and the identification of natural and electroconvective flow phenomena. These capabilities underscore its strong potential as a high-resolution, dynamic diagnostic platform for investigating mass transfer processes at electrochemical interfaces.

2.4. Consistency verification and parameter inversion

Once reliable interferometric data have been obtained, the research focus shifts to how these results can be used to validate or refine theoretical models of mass transport. The core strategy is to treat the reconstructed concentration field as a calibration constraint, compare it point-by-point with model predictions, and retrieve key parameters such as diffusion coefficients by curve fitting.[86]

Under conditions of restricted diffusion or in the initial stage of galvanostatic operation, the analytical solutions of the Nernst–

Planck or Fick diffusion equations provide the classical boundary layer scaling relation ($\delta \sim \sqrt{Dt}$) and error-function-type concentration profiles. In such cases, experimentally measured concentration distributions $c(x, y, t)$ or boundary layer thickness $\delta(t)$ can be directly used to extract diffusion coefficients.[87–89] Under isothermal conditions with known boundary flux, ionic transference numbers can also be determined by combining electroneutrality constraints with conductivity relations.[90,91]

When residuals between model and experiment exhibit consistent spatial or temporal structures, they often indicate "missing physical processes". For example, residuals showing thicker-than-expected boundary layers near the electrode typically suggest that buoyancy-driven natural convection cannot be neglected.[88,92] Residuals that increase nonlinearly with bulk concentration point to concentration-dependent diffusion coefficients $D(c)$ or transference numbers $t(c)$.[90] Residuals that evolve with time and correlate with current density likely reflect coupled processes such as momentum lag or electroconvection.[89] This diagnostic pathway, from residual patterns to physical model augmentation, helps avoid systematic errors that would otherwise arise from incorrectly attributing convective or thermal effects to diffusion coefficients or transference numbers.

Beyond parameter fitting, experimental $c(x, y, t)$ fields can also be compared frame by frame with multiphysics numerical simulations. On the one hand, missing physical processes can be introduced into the model, such as incorporating transport properties of specific ions or applying turbulence models to account for convective transport.[86,93] On the other hand, key parameters can be iteratively fitted so that simulated concentration fields converge toward experimental observations.[94] Sensitivity-based ranking allows the most influential parameters on concentration distribution to be prioritized in fitting, enabling significant predictive gains with minimal model complexity.

3. Representative application of laser interferometry in electrochemical interface studies

In this section, the application of laser interferometry to the characterization of electrode-electrolyte interfacial phenomena in electrochemical systems is systematically reviewed. Representative studies are examined in detail, and comparisons are made in terms of experimental configurations, data processing methodologies, and the interfacial transport mechanisms that are revealed. According to the primary research objectives and the characteristic features of interfacial mass transport behavior, existing applications can be broadly categorized into the following four typical scenarios.

3.1. *In situ* observation of interfacial concentration field evolution

The application of laser interferometry for observing concentration fields in electrochemical systems dates back to the 1960s. In 1967, Knox and co-workers first reported its use in monitoring the anodic dissolution of iron in sulfuric acid and copper electrodeposition in a copper sulfate solution.[23] As shown in Fig. 3(a), they visualized the temporal evolution of interference fringes, thereby intuitively revealing the development of interfacial concentration gradients and diffusion layer thickness. This work validated the feasibility of optical interferometry for *in situ* electrochemical analysis.

In 1973, Newman *et al.* further extended the method by coupling it with a classical restricted diffusion model to study the relaxation of concentration gradients in binary electrolytes.[26] As depicted in Fig. 3(b), they established an analytical framework that inverted concentration profiles from interferograms and extracted diffusion coefficients *via* numerical fitting, achieving a measurement error below 0.2%. This work demonstrated the high precision and repeatability of interferometric techniques for quantifying limited diffusion processes. Subsequently, McLarnon and colleagues employed a dual-beam interferometric system to systematically investigate diffusion layer evolution during metal electrodeposition under galvanostatic conditions.[27] Their approach enabled quantitative reconstruction of both the normal concentration profile perpendicular to the electrode surface (Fig. 3(c)) and the tangential profile near the interface (Fig. 3(d)). The study revealed that as the interfacial concentration approached zero (*i.e.*, under limiting diffusion), the cell voltage rose rapidly, which is consistent with predictions from diffusion theory. This provided strong evidence for the coupling between the interfacial concentration distribution and the electrochemical potential response. Furthermore, the nonlinear concentration dependence of the diffusion coefficient was revealed *via* numerical fitting, and cation transference numbers were calculated, offering key parameters for modelling interfacial mass transport.

In the 21st century, this technique has been extended to a broader range of systems. In 2003, Ota *et al.* applied optical interferometry to a $LiClO_4$-propylene carbonate (PC) system to monitor the evolution of the Li^+ concentration boundary layer during lithium deposition.[87] As shown in Fig. 3(e), at a low current density, the fringe pattern remained nearly stationary in the initial stage, indicating a pronounced induction period. A linear relationship between the boundary layer thickness δ and $\sqrt{t}$ (Fig. 3(f)) confirmed that this period corresponds to a pre-diffusion regime (with $\delta \approx 0$), whose duration increases significantly at lower current densities. Further analysis in Fig. 3(g) shows excellent agreement between experimental data and theoretical predictions for boundary layer growth (solid lines: theory; symbols: measured values), validating that δ increases in accordance with natural convection-driven mass transfer under high-current conditions. In a complementary study, Nishikawa and colleagues investigated lithium deposition in a $LiPF_6$-PC electrolyte system, with a focus on how current density influences both solid electrolyte interphase (SEI) formation and Li^+ boundary layer development.[96] Their findings

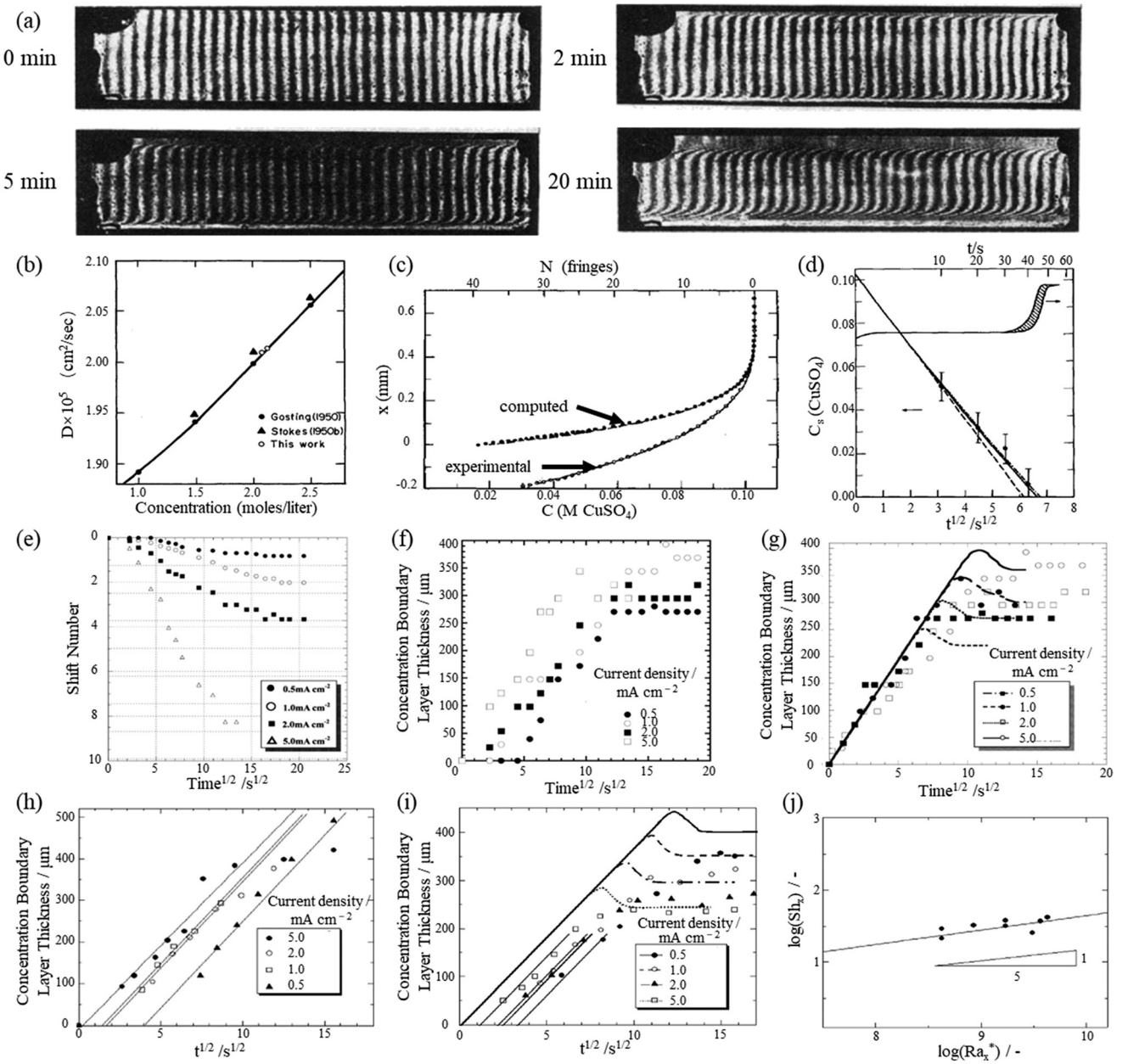

Fig. 3 Representative applications of laser interferometry for characterizing electrode–electrolyte interfacial concentration fields. (a) Example interferograms recorded, demonstrating fringe shifts induced by concentration variations.[23] Panels show the fringe evolution at 0, 2, 5, and 20 minutes under constant electrochemical conditions. Adapted from ref. 23 with permission from the American Chemical Society, copyright. (b) Diffusion coefficient of potassium chloride in aqueous solution at 25 °C, determined through interferometric measurements with a reported error margin below 0.2%.[26] Reproduced from ref. 26 with permission from Wiley, copyright. (c and d) Interfacial concentration fields reconstruct:[27] (c) Normal concentration profile perpendicular to a downwards-facing cathode (hollow circles: experimental values; dashed line: fitted profile; solid circles: corrected computational values; solid line: fitted curve). (d) Transient interfacial concentration *versus* time, with simultaneous monitoring of cell voltage evolution. Reproduced from ref. 27 with permission from Elsevier, copyright. (e–g) Results from the lithium deposition experiments:[87] (e) Time evolution of the number of interference fringes N at different current densities, (f) linear relationship between boundary layer thickness δ and $\sqrt{t}$, (g) comparison between experimental δ values and theoretical predictions accounting for Li^+ diffusion and natural convection (symbols: experiments; solid lines: model fits). Reproduced from ref. 87 with permission from Elsevier, copyright. (h–j) Experimental observations of concentration boundary layer evolution and associated transport behavior:[95] (h) Time-dependent evolution of the anodic concentration boundary layer in a horizontal cell configuration, (i) corresponding behavior under a vertical configuration, showing saturation of boundary layer growth, (j) log–log plot of the Sherwood number (Sh_x) *versus* the modified Rayleigh number (Ra_x^*), exhibiting power-law scaling. Reproduced from ref. 95 with permission from Elsevier, copyright.

revealed that interfacial concentration dynamics play a critical role in determining the duration of the induction period and in modulating subsequent electrochemical kinetics.

In their investigation of lithium metal dissolution in PC-$LiClO_4$ electrolytes, Nishikawa *et al.* systematically evaluated the role of natural convection in mass transport under different cell orientations.[95] As shown in Fig. 3(h), in the horizontal configuration, the measured boundary layer thickness closely matched predictions from a one-dimensional transient diffusion model, suggesting that mass transfer was diffusion-dominated. To further probe the convective effects, the researchers switched to a vertical configuration. Fig. 3(i) reveals a pronounced plateau in boundary layer growth, indicating saturation over time. This behavior was attributed to natural convection triggered by local $LiClO_4$ accumulation, which perturbed the purely diffusive transport regime. Under higher current densities, this saturation became more evident and aligned better with natural convection mass transfer models. To quantify the transition, the authors introduced a regression relationship between the Sherwood number (Sh_x) and the modified Rayleigh number (Ra_x^*) in logarithmic coordinates (Fig. 3(j)), finding that Sh_x is proportional to Ra_x^* to a power of 1/5. This result validates the presence of convection-driven transport in this system and is consistent with classical theories of natural convection boundary layers. This study stands out as one of the earliest systematic demonstrations of how natural convection can significantly influence the evolution of concentration fields at electrochemical interfaces, offering theoretical support for later modelling efforts involving coupled multiphysical fields.

In summary, although early studies relied primarily on fringe displacement for simplified quantitative analysis with limited post-processing accuracy, laser interferometry nonetheless proved capable of effectively characterizing key interfacial mass transport parameters such as concentration gradients and diffusion layer thickness. Particularly in complex scenarios where natural convection is present, the observed evolution of the concentration profiles is strongly consistent with that of the theoretical models. These results underscore the practical utility and reliability of interferometric imaging for real-time, *in situ* visualization of electrochemical interface dynamics.

Building on conventional laser interferometry, DH has recently been widely applied for high-resolution, *in situ* monitoring of concentration fields in diverse electrochemical systems. Unlike earlier methods that relied on grayscale fringe images or localized linear approximations, DH enables full-field recovery of phase information, allowing for real-time, quantitative reconstruction of two-dimensional concentration fields with improved temporal resolution and spatial consistency. Researchers have successfully implemented DH in lithium-ion, zinc-ion, and flow battery systems to visualize the dynamic evolution of boundary layers, quantify local concentration gradients and diffusion thicknesses, and verify or extend classical diffusion models.[32,36,37,88,97–101] For example, as illustrated in Fig. 4, Yuan *et al.* first recorded the evolution of interference fringes (Fig. 4(a)) and subsequently reconstructed a

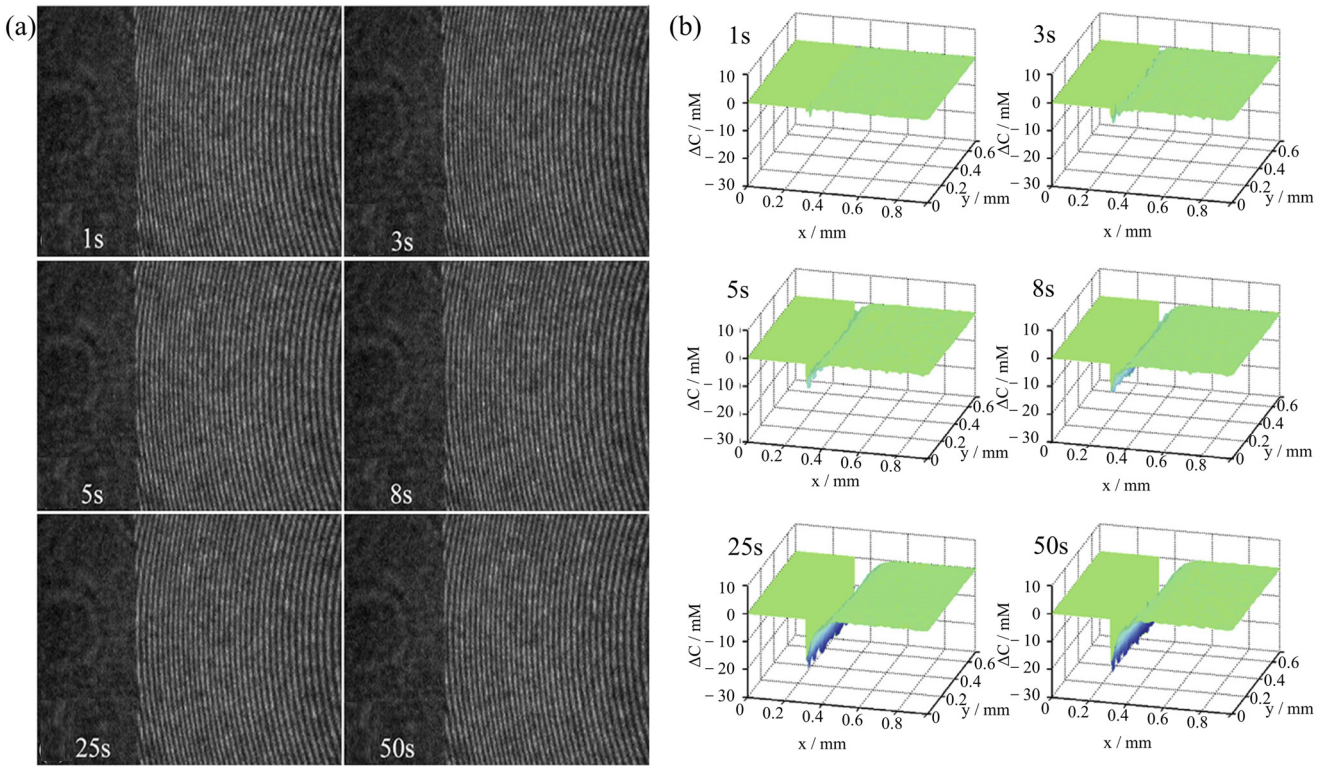

Fig. 4 Dynamic tracking of interfacial concentration fields *via* digital holography:[37] (a) time-resolved interferograms showing fringe evolution. (b) Corresponding 2D concentration maps reconstructed from the phase information in (a). Adapted from ref. 37 with permission from Elsevier, copyright.

sequence of concentration fields (Fig. 4(b)), capturing the transition from an initially uniform distribution to the formation of interfacial boundary layers. This demonstrates the strength of digital holography (DH) in tracking interfacial dynamics.[37]

Lai *et al.* further applied this method to a graphite/Li half-cell system, coupling cyclic voltammetry (Fig. 5(a)) with phase field reconstruction at selected potentials (Fig. 5(b)).[38] Their study successfully identified the multistage formation pathway of the SEI layer and revealed how lithium co-insertion/extraction and gas evolution behavior in PC-based electrolytes correlate with abrupt interfacial concentration changes. Cross-verification with XPS confirmed the linkage between the concentration field evolution and interfacial reaction products. In lithium-sulfur systems, Dai *et al.* employed cyclic voltammetry (Fig. 5(c)) in conjunction with 2D phase maps (Fig. 5(d)) to visualize the dissolution, diffusion, and re-deposition of lithium polysulfides (Li_2S_n) during the charge/discharge process.[39] Their results confirmed that periodic oscillations in the concentration field were induced by the shuttle effect, providing direct experimental insight into its spatiotemporal dynamics. In aqueous zinc batteries, Li *et al.* evaluated the regulatory effect of 1-hydroxyethane-1,1-diphosphonic acid (HEDP) on the Zn^{2+} concentration distribution and zinc deposition morphology.[40]

As shown in Fig. 6(a), the presence of HEDP increased the initial overpotential and stabilized the voltage behavior, indicating delayed nucleation and smoother deposition. The phase field maps (Fig. 6(b)) confirmed suppressed concentration heterogeneity and a more stable diffusion layer in the presence of HEDP (i′–iv′) than in the additive-free case (i–iv). The corresponding SEM images (Fig. 6(c and d)) further verified the relationship between the concentration field uniformity and electrode surface morphology. Xu *et al.* advanced this work by achieving spatiotemporal reconstruction of Zn^{2+} concentration fields, demonstrating that the homogeneity of ion distribution is directly coupled to interfacial deposition behavior.[41] These findings provide crucial concentration-field-based insights for interfacial structure design in electrochemical systems.

In a recent representative study, Kamesui *et al.* employed a commercial digital holographic microscope (Lyncee Tec) to perform high-resolution, full-field, *in situ* visualization of interfacial concentration gradients and relaxation behavior in a lithium bis(fluorosulfonyl)imide-tetraglyme (LiFSA-G4) solvate ionic liquid system.[102] Interference patterns from both the anode and cathode regions were recorded simultaneously. As shown in Fig. 7(a), the phase map captured during the galvanostatic electrolysis stage (0–100 s) clearly illustrates the development of interfacial concentration gradients. Upon cessation of the current, the system transitioned into a natural

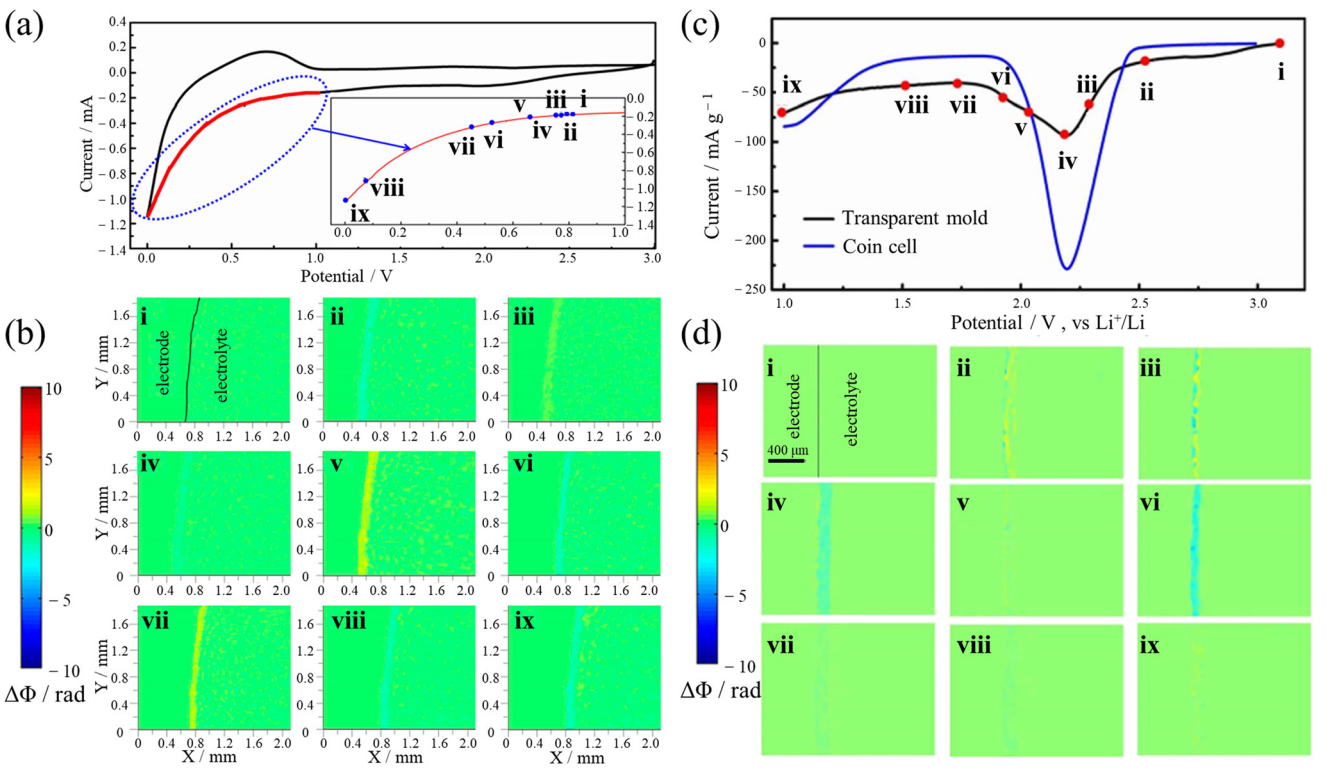

Fig. 5 Representative studies coupling cyclic voltammetry and interferometric imaging for interfacial concentration dynamics. (a and b) *In situ* visualization of a graphite/Li half-cell:[38] (a) CV curves indicating key reaction processes and (b) 2D phase maps at selected potentials (i–ix) corresponding to the states in (a). Adapted from ref. 38 with permission from the American Chemical Society, copyright. (c and d) Visualization of the shuttle effect in lithium-sulfur batterie:[39] (c) CV curves of sulfur/carbon nanotube composites in a transparent model cell and a coin cell and (d) 2D phase maps at selected potentials (i–ix) corresponding to the states in (c). © The Electrochemical Society. Adapted by permission of IOP publishing. All rights reserved. Source: ref. 39.

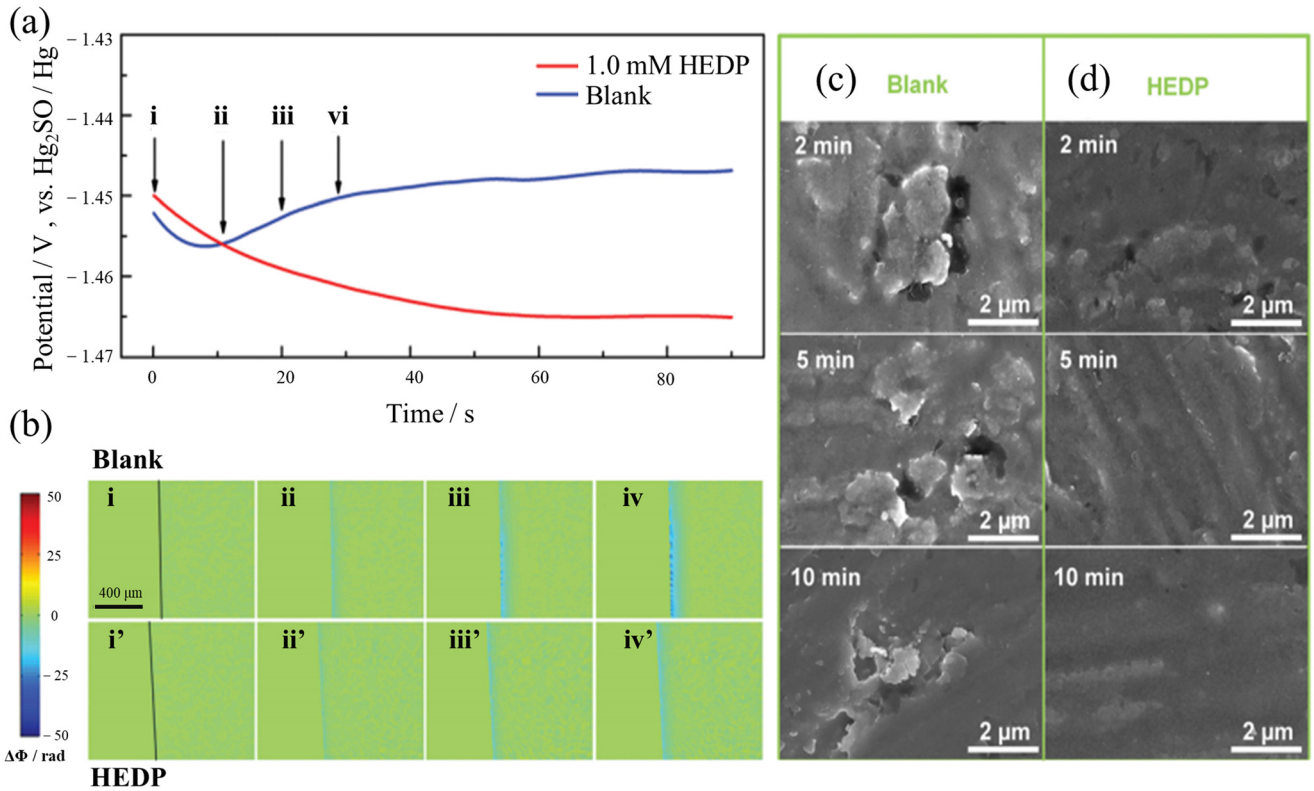

Fig. 6 Investigation of HEDP additive effects on zinc deposition in aqueous Zn batteries:[40] (a) Voltage responses under constant current with and without HEDP. (b) Corresponding 2D phase field distributions at selected potentials, where (i–iv) correspond to the time points indicated in (a) without HEDP, and (i′–iv′) correspond to the same time points with HEDP. (c and d) SEM images of Zn deposits formed (c) without and (d) with HEDP, respectively. Adapted from ref. 40 with permission from Wiley, copyright.

relaxation regime (Fig. 7(b)). Further quantitative analysis of the concentration evolution at the anode and cathode sides is shown in Fig. 7(c) and Fig. 7(d). In both cases, δ exhibits a strong linear correlation with $\sqrt{t}$, indicating that diffusion remains the dominant interfacial mass transport mechanism during both the electrolysis and natural relaxation stages. The researchers coupled the refractive index, concentration, and viscosity relationships to reconstruct the local viscosity distribution of the electrolyte based on the acquired phase maps. The reconstructed viscosity fields are shown in Fig. 7(e) and (f). Their analysis revealed that the observed spatial asymmetry in the concentration field is attributable primarily to variations in the electrolyte viscosity: the viscosity near the anode was significantly higher, which in turn reduced Li^+ mobility and intensified concentration retention and gradient accumulation at the interface. This phenomenon highlights the critical influence of local physicochemical properties, such as viscosity, on ion transport efficiency and the spatiotemporal evolution of interfacial concentration fields. This finding also suggests that future electrolyte design should account not only for electrochemical stability but also for fluidic properties. Overall, this study not only reinforced the high spatial and temporal resolution of digital holographic interferometry in tracking transient diffusion behavior in electrochemical systems but also demonstrated its unique ability to resolve coupled concentration and property fields simultaneously. These findings provide strong experimental support for further investigations into ion migration mechanisms and for the rational optimization of electrolyte parameters.

To summarize, early studies have demonstrated that laser interferometry enables *in situ*, dynamic visualization of concentration field evolution at electrochemical interfaces. Whether under purely diffusion-controlled conditions or within more complex environments involving multi-ion systems and coupled physical fields, this technique has proven effective in capturing concentration gradient dynamics and validating transport models. With the development of digital holography, which offers enhanced spatial resolution, faster temporal responsiveness, and more accurate data reconstruction, the methodology has evolved into a powerful tool for probing interfacial processes. This approach not only supports quantitative analysis of mass transport behavior but also facilitates the concurrent evaluation of auxiliary parameters such as viscosity. As such, laser interferometric imaging is becoming an increasingly important technique for electrochemical interface diagnostics and electrolyte system optimization.

3.2. Visualization of metal deposition dynamics and dendrite growth

While the studies discussed in the previous section focused primarily on diffusion layer evolution near planar electrodes,

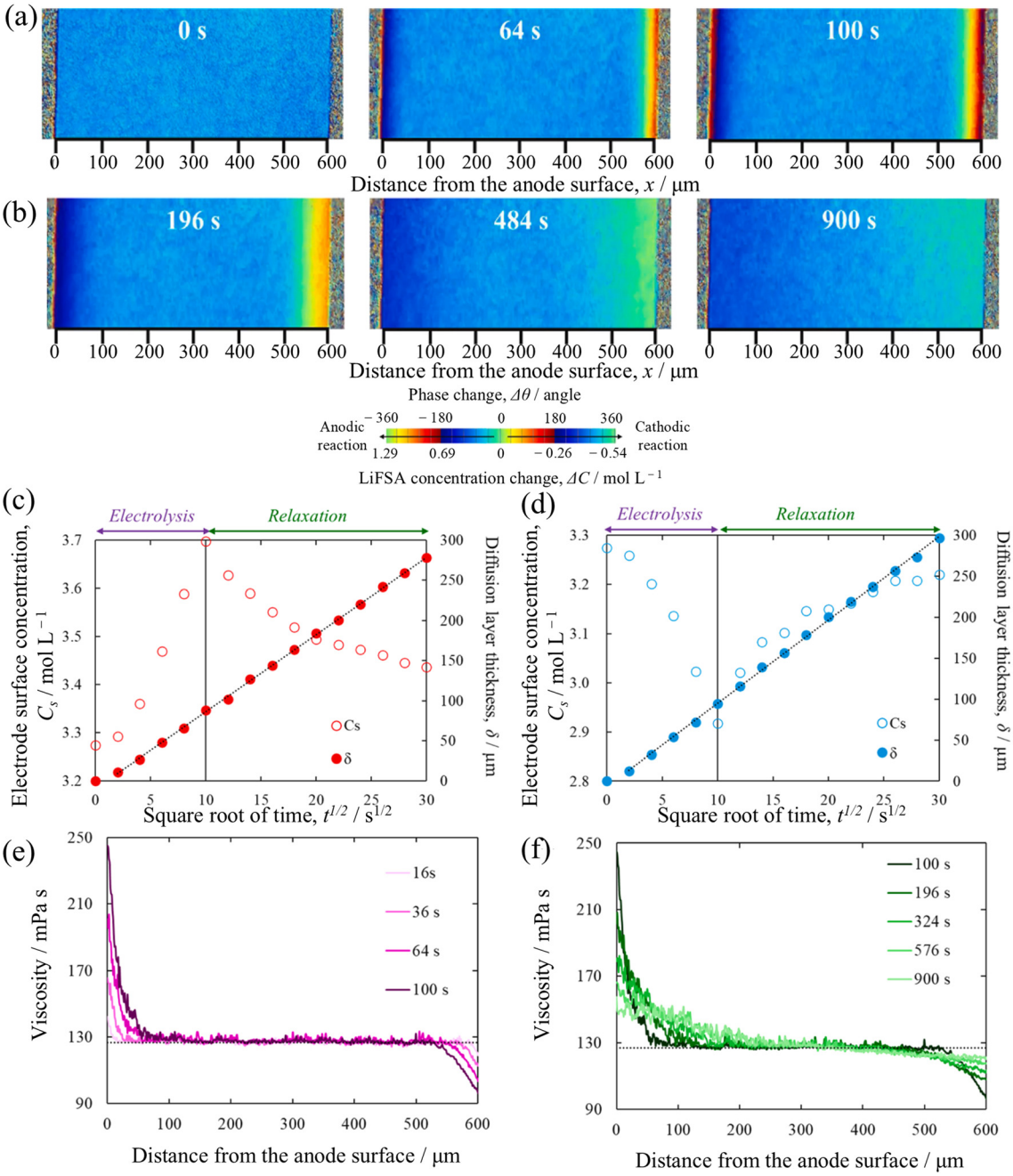

Fig. 7 Two-dimensional concentration and viscosity field reconstruction in lithium salt solvate ionic liquid systems using DH.[102] (a and b) Phase holographic reconstruction: phase distribution during (a) galvanostatic electrolysis stage (0–100 s) and (b) natural relaxation stage (>100 s), where the color map corresponds to the LiFSA concentration. The dotted regions on the left and right represent the anode and cathode, respectively, whereas the light blue central area represents the electrolyte. (c and d) Time-dependent evolution of the interfacial concentration (hollow circles) and diffusion layer thickness (solid circles) at the (c) anode and (d) cathode. (e and f) Spatial distribution of the electrolyte viscosity reconstructed from concentration–viscosity correlation during (e) electrolysis and (f) relaxation. Adapted from ref. 102. This article is an open access article under the terms of the Creative Commons CC-BY license.

investigations on non-uniform growth fronts, particularly the coupled concentration-morphology-kinetics behavior during dendritic metal deposition, remain relatively limited. In metal electrodeposition, especially in systems where dendritic structures form and evolve, the local concentration field plays a critical role in dictating the deposition process, surface morphology, and associated dynamics. Owing to the highly irregular geometry of dendrites, their complex electric and concentration field distributions, and the interplay with convective effects, traditional modelling approaches often fall short in accurately predicting growth behavior. Laser interferometric techniques, which enable direct visualization of the local concentration fields around dendrite tips, provide a valuable experimental tool to probe the underlying

mechanisms of dendrite formation and its coupling with mass transport phenomena.

Fukunaka *et al.* applied laser holography to *in situ* monitor Ag dendrite growth in $AgNO_3$ solutions and successfully quantified local concentration gradients and ion transport behavior at dendrite tips.[103] This work laid the foundation for the application of interferometry to non-steady-state dendritic systems. Subsequently, Barkey and co-workers compared the evolution of concentration fields during copper and zinc electrodeposition under vertical and horizontal electrode configurations.[28] By reconstructing concentration profiles from interferograms, they analysed how natural convection patterns vary with cell orientation and demonstrated the coupling between local concentration distributions and dendritic morphology. Their study revealed that in the vertical configuration, natural convection tends to be more pronounced, enhancing ion transport toward dendrite tips and promoting tip splitting and unstable growth (Fig. 8(a)). In contrast, under horizontal configurations, natural convection is suppressed, but electroconvection may be triggered under conditions of high voltage and low electrolyte concentration, leading to the formation of channel-like, parallel dendritic structures (Fig. 8(b)). Further concentration field analysis confirmed that distinct morphologies are associated with differing interfacial concentration patterns in each configuration, directly influencing dendritic branch selection and overall morphological evolution.

Argoul *et al.* systematically investigated zinc dendrite formation in a thin-layer electrochemical cell without a supporting electrolyte.[30] By employing a feedback-coupled interferometric system (Fig. 8(c)), researchers have directly captured iso-concentration contours at the electrode interface. Under high-field conditions ($[ZnSO_4]$ = 0.5 mol L^{-1}, j = 150 mA

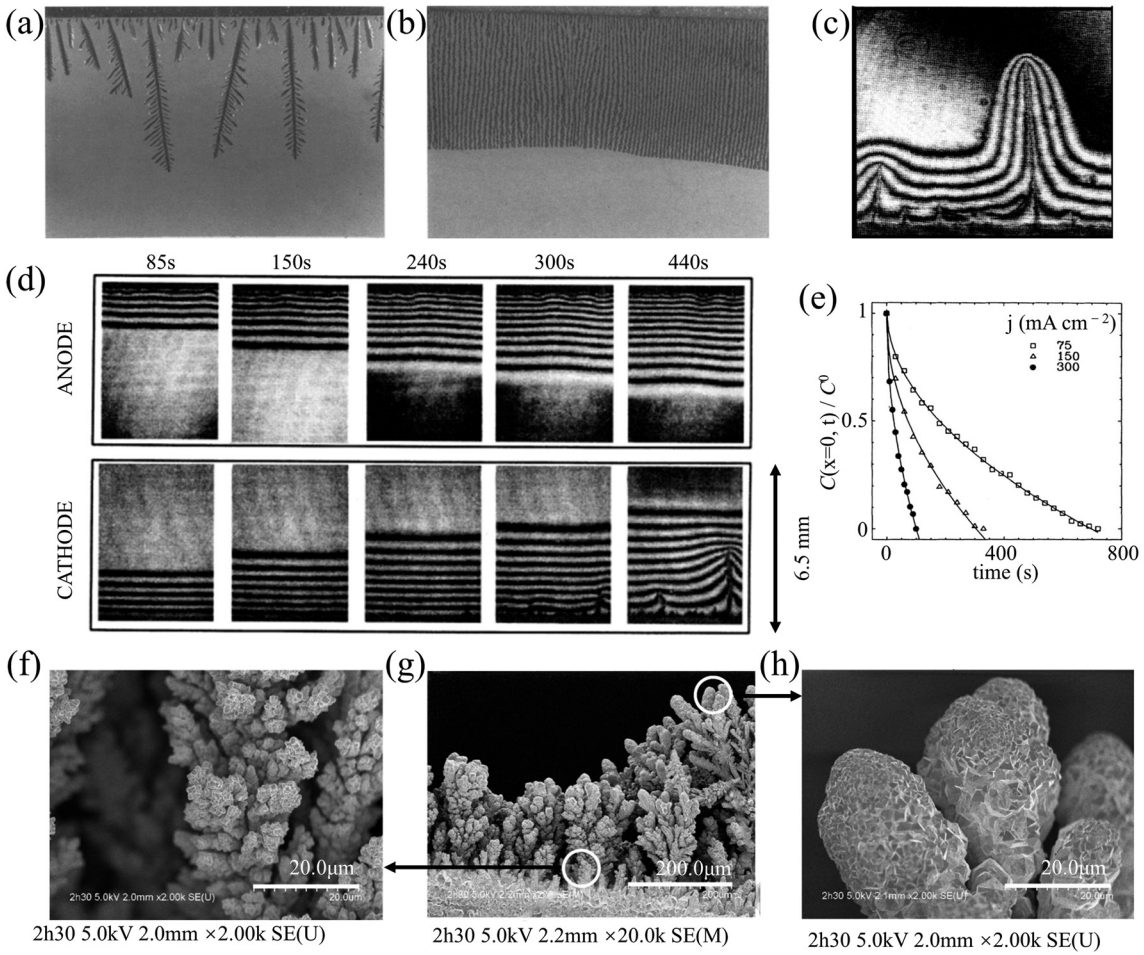

Fig. 8 Interferometric visualization of dendritic growth and associated concentration fields. (a and b) Two types of dendritic growth:[28] (a) tip splitting and unstable growth under strong natural convection (vertical configuration) and (b) channel-like parallel dendrites under suppressed convection but induced electroconvection (horizontal configuration). © The Electrochemical Society. Adapted by permission of IOP publishing. All rights reserved. Source: ref. 28. (c) Interferometric imaging of local concentration fields around zinc dendrites during electrodeposition.[30] (d) Time-lapsed interferograms showing morphological evolution in a thin-gap electrochemical cell: t = 85, 150, 240, 300 and 440 s.[30] (e) Time-dependent evolution of the interfacial concentration $[ZnSO_4]_{x=0}/[ZnSO_4]_0$ under different current densities, as quantitatively measured.[30] Reproduced from ref. 30. With permission from the American Physical Society, copyright. (f–h) SEM observations revealed detailed dendritic morphologies:[54] in the early stage (bottom of (g), or (f)), loosely packed mossy deposits formed near the cathode. In the later stage (top of (g) or (h)), the dendrite tips developed into more compact and orderly microstructures. Adapted from ref. 54 with permission from Elsevier, copyright.

cm^{-2}), the dendrite tip with the fastest growth rate was observed to capture most of the local current density, effectively shielding neighboring branches. Dense fringe patterns at the dominant tip indicate a steep local concentration gradient, which is correlated with a high deposition rate. The time-sequenced interferograms in Fig. 8(d) reveal the spatiotemporal evolution of the deposition process. In the early stage (85–240 s), symmetrical fringe patterns emerged from both electrodes, suggesting diffusion-dominated transport. As deposition progressed (240–440 s), multiple sharp dendrites grew from the cathode, distorting the initial flat contours and indicating interfacial instability. Once a leading dendrite gains an advantage, it continues to dominate growth and inhibits adjacent branches *via* electric field shielding. Simultaneously, asymmetric ion release from anodic metal oxidation caused deviations from symmetry in the concentration field. Further analysis of the concentration evolution under varying current densities (Fig. 8(e)) revealed that high current densities significantly enhanced natural convection, which in turn accelerated ion transport, increased concentration field inhomogeneity, and intensified the growth dominance of leading dendrites.

In follow-up work, Léger and colleague developed a nonlinear diffusion model incorporating concentration-dependent diffusion coefficients and transference numbers.[31,56] Their model successfully described the evolution of dendrites with greater accuracy. They reported that once the electrolyte layer exceeded 70 μm, buoyancy-driven natural convection significantly altered the local concentration fields, affecting both the dendrite propagation velocity and growth stability. In more complex systems, Nishikawa *et al.* combined laser interferometry with SEM imaging to investigate morphological transitions in copper deposition under unsupported electrolyte conditions.[54] Initially, a relatively uniform interfacial concentration gradient ensured a sufficient ion supply, promoting rapid, multibranched dendritic growth and the formation of loose moss-like structures (Fig. 8(f)). As deposition continued, the dominant dendrites increasingly captured the current, resulting in sharper tip gradients and the suppression of surrounding branches. The leading edge developed more compact and regular microstructures (Fig. 8(h)). These morphological changes closely matched the concentration field observations, confirming a strong coupling between the concentration dissipation rate and deposition morphology. The study elucidated a transition from fast powdery deposition to slow dense growth, highlighting how the growth rate is modulated by ion depletion dynamics.

In recent advances, research teams led by Miki and Kamesui applied DH to lithium dendrite studies, focusing on the role of solvation structures in highly concentrated nonaqueous electrolytes.[42,104] Their work quantitatively revealed how local concentration gradients, viscosity variations, and solvent properties regulate dendrite microstructural stability. They reported significant regional differences in electrolyte viscosity and Li^+ transport capability and demonstrated that local inhomogeneities in concentration were directly reflected in dendrite morphology and granularity. These findings suggest a new pathway for morphology control *via* electrolyte physical properties, offering valuable design insights for advanced lithium metal batteries.

In summary, both laser interferometry and digital holography have demonstrated exceptional capabilities for real-time, high-resolution visualization of concentration fields during metal electrodeposition, particularly for dendritic growth. By integrating dynamic concentration mapping with morphological analysis, these techniques have allowed researchers to uncover the intricate effects of concentration gradients, convection, and electrolyte properties on dendrite growth kinetics and stability. These insights not only deepen the fundamental understanding of electrodeposition processes but also offer practical guidance for the design of dendrite-suppressing strategies and the optimization of electrode–electrolyte systems. Furthermore, they pave the way for more accurate multiphysics models of electrochemical interfaces by incorporating concentration-field dynamics into morphological and kinetic predictions.

3.3. Visualization of mass transfer and corrosion behavior under magnetohydrodynamic effects

Magnetic fields influence interfacial mass transport in electrochemical systems by inducing magnetohydrodynamic (MHD) effects through Lorentz forces. This process entails strong coupling and nonlinear interactions among concentration, flow, electric, and magnetic fields, posing substantial challenges for conventional modelling approaches that rely on simplifications. This complexity makes it one of the most challenging and important application fields of laser interferometry technology in electrochemical systems.

As early as the 1980s and 1990s, O'Brien, Santhanam, and coworkers conducted foundational studies on magnetic field-regulated interfacial mass transfer.[24,25,105] They developed various static and rotating electrode configurations to systematically investigate interfacial flow structures induced by Lorentz forces under both perpendicular and parallel magnetic fields. These studies characterized the spatial features of MHD flow near the electrode surface and demonstrated its profound influence on the diffusion layer thickness, interfacial concentration gradient, and spatial distribution of the current density. This body of work lays the experimental groundwork for subsequent *in situ* interferometric studies of MHD-driven mass transport phenomena.

In 1994, Wang *et al.* employed laser interferometry to *in situ* monitor the anodic dissolution of iron in sulfuric acid, with a particular focus on how MHD flows induced by a perpendicular magnetic field influence the dynamics of the concentration boundary layer.[106] Their results revealed that shear convection induced by MHD flows could dramatically alter the diffusion layer thickness and modulate the balance between oxide film formation and dissolution. To expand this research, Wang's team explored electrochemical systems that exhibit oscillatory current behavior.[107] They discovered that MHD effects, induced by the magnetic field, significantly increased mass transfer rates and intensified concentration perturbations, thereby disrupting the conditions required for

sustained film growth at the electrode surface. This effectively suppressed the system's inherent oscillatory behavior. In further studies, they examined the natural relaxation process of diffusion layers following electrode passivation.[108] The findings indicated that MHD effects, induced under magnetic fields *via* Lorentz forces, could delay diffusion layer relaxation, thereby affecting both passivation and reactivation of the electrode. Collectively, Wang's body of work highlighted the unique ability of laser interferometry to dissect multiphysics coupling between magnetic fields, mass transfer, and interfacial phenomena. These studies not only extended the depth of interferometric applications but also established a clear experimental paradigm and analytical framework for exploring interfacial dynamics in complex magnetic field environments.

Overall, a widely adopted framework for analysing interfacial behavior under magnetic fields involves the use of characteristic potentials from polarization curves as reference points for interpreting reaction pathways and concentration dynamics. In this context, Yuan *et al.* employed digital holography to visualize, *in situ*, the corrosion process of copper in a Cu/NaCl system, focusing on the formation of CuCl products.[36,98] Phase reconstruction clearly revealed localized concentration disturbances and flow structures under MHD influence. As shown in Fig. 9, under zero magnetic field (Fig. 9(a)), the anodic dissolution of copper proceeded in a diffusion-controlled manner. Initially, Cu^{+} release led to increased interfacial concentration (expanding red regions in the phase map). As the potential increased, Cl^{-} consumption induced CuCl precipitation, and a decrease in the interfacial concentration was reflected by the emergence of blue zones. In the final stage, Cu^{2+} formation led to a stabilized diffusion layer (homogeneous red zone), indicating enhanced interfacial stability under dominant diffusion. Upon application of a 450 mT perpendicular magnetic field (Fig. 9(b)), the MHD effects significantly altered the mass transport dynamics. During the CuCl formation stage, MHD-enhanced convective migration of Cu^{+} and Cl^{-} ions suppressed salt layer precipitation, as evidenced by an ~30% reduction in the blue region area compared with that in the no-field case. In the Cu^{2+} formation phase, downwards vortex-like flow emerges at the electrode center, and the red region spirals outwards, indicating enhanced 3D transport and a >40% reduction in the interfacial concentration gradient. This mass transport intensification led to a marked increase in the current density within the polarization plateau region to twice the value under zero-field conditions, thus confirming the role of magnetic fields in promoting interfacial exchange and suppressing localized corrosion.

Subsequent studies by Liu *et al.*[110] and Xu *et al.*[41] further revealed that in grain boundary-sensitive corrosion systems, magnetic fields not only accelerated boundary dissolution but also facilitated intergranular propagation. These findings suggest that MHD effects extend beyond modifying diffusion

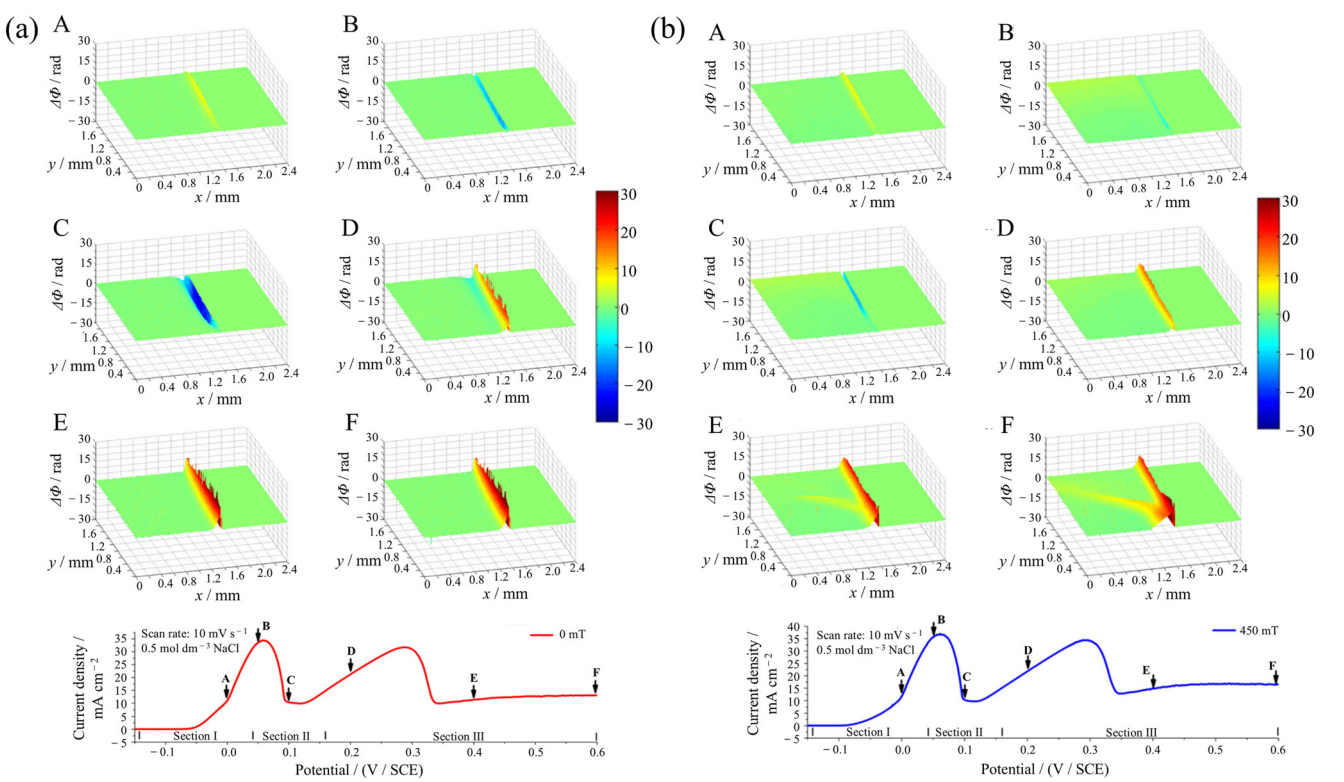

Fig. 9 Evolution of phase maps at different polarization potentials during the anodic dissolution of copper.[109] (a) Without a magnetic field: panels (A–F) correspond to points A–F on the polarization curve below. (b) With a perpendicular magnetic field (450 mT, inducing MHD effects): panels (A–F) correspond to points A–F on the polarization curve below. Adapted from ref. 109 with permission from Elsevier, copyright.

alone and may also reshape local corrosion pathways and mechanisms, highlighting their potential in corrosion morphology regulation.

In summary, MHD effects, induced by Lorentz forces under magnetic fields, regulate electrochemical interface behavior by modifying the diffusion layer structure, convective flow, and corrosion film dynamics. Laser interferometry, particularly digital holography, has proven to be an accurate and high-throughput platform for *in situ* investigation of these magnetically influenced phenomena. It is particularly effective for visualizing the spatiotemporal evolution of complex concentration fields under MHD conditions. This methodology not only broadens the scope of electrode process analysis but also provides experimental support and theoretical foundations for the design of magnetic-field-assisted corrosion mitigation strategies.

3.4. Multimodal integration for multi-parameter and synergistic interfacial measurements

Before discussing multimodal integration strategies, it is necessary to clarify the current technical bottlenecks facing laser interferometry in electrochemical interface studies. (1) Thickness-averaging limitations: most existing interferometric systems employ a single transmission path and record integrated phase changes across the electrolyte. As a result, they provide only thickness-averaged concentration values along the optical axis and fail to resolve layered microstructures at the micron scale. This leads to what is known as the thickness-averaging effect. Notably, even systems claiming to use digital holography have not fundamentally overcome this limitation in most electrochemical studies. (2) Inability to distinguish ionic species: since interferometric signals reflect total refractive index changes, they cannot be used to differentiate contributions from individual ionic species. In multi-ion systems, this can lead to significant misinterpretation of concentration distributions. (3) Optical system constraints: to ensure clearly resolvable fringe patterns, the electrolyte must be highly transparent, low-scattering, and chemically stable. Systems containing precipitates, gas bubbles, nanoparticles, or viscous solvents pose serious challenges to measurement fidelity. (4) Environmental sensitivity: interferometric systems are highly susceptible to external disturbances. Gas evolution, convective flow, or temperature gradients can disrupt the optical path, introducing complex and often uncontrollable phase noise into the reconstruction process. (5) Limited compatibility with porous electrodes: conventional transmission-mode interferometry is inherently ill suited for probing ion transport and localized deposition within three-dimensional porous electrodes.

To overcome the above limitations, researchers have progressively developed hybrid systems that integrate laser interferometry with other imaging or analytical methods, enabling simultaneous and coupled analysis of concentration fields, flow dynamics and interfacial morphology. Early efforts by Huth *et al.* combined laser interferometry with particle image velocimetry (PIV) to study coupled concentration-flow field behavior during electrodeposition in a $ZnSO_4/CuSO_4$ system.[29] As shown in Fig. 10(a), the particle tracking data and interferometric phase maps jointly revealed that off-normal concentration gradients act as the primary driving force for buoyancy-induced convection. In addition, Nishikawa's group further integrated PIV, laser scanning confocal microscopy (LSCM), and optical absorption imaging into lithium and copper systems.[111,112] These approaches enabled dynamic reconstruction of specific ionic concentrations and revealed a direct correlation between ion transport behavior and electrode volume changes. Through combined analysis of LSCM images at different lithiation stages (Fig. 10(b)) and electrochemical measurements, a semi-quantitative relationship was established between Li^+ transport kinetics and surface morphology evolution. Tada *et al.* coupled interferometry with shadowgraphy, a contrast-enhancement imaging technique that visualizes refractive index gradients based on light deflection, to investigate Zn^{2+} transport dynamics. The spatial localization of Zn^{2+} deposition was further validated using electrochemical microscopy (SECM), demonstrating precise mapping of metal-ion accumulation.[113]

In more recent work, Kamesui[42,101,102] and Miki[104] have expanded integration strategies to include *in situ* Raman spectroscopy, X-ray tomography, and finite difference simulations. For example, as shown in Fig. 10(c–f), Raman spectra provided insights into the solvation structure and Li^+ coordination environment in different electrolyte formulations. When combined with concentration gradient data obtained from interferometry, this enables the construction of a triply coupled model with a concentration–viscosity–solvation structure. This model not only elucidates the intrinsic regulatory relationship between the diffusion coefficient, migration number and ion solvation clusters but also allows for a cross-scale correlation between the ion migration behavior and interfacial morphology.

In essence, multimodal integration has become a key strategy for extending the capabilities of conventional interferometry and achieving multiscale-multiphysics reconstructions at electrochemical interfaces. With hardware synchronization and data fusion strategies, multiple physical parameters, including concentration, velocity, temperature, and potential, can be mapped onto a unified spatiotemporal coordinate framework, enabling multidimensional, *in situ* visualization of interfacial reactions, mass transport, and morphological evolution.

To summarize, the ability of the integration of laser interferometry with complementary imaging and analytical techniques has greatly expanded its ability to resolve complex interfacial processes. These multimodal approaches offer unique advantages in overcoming current limitations, such as three-dimensional field reconstruction, species decoupling, and the analysis of coupled multiphysical effects. Coupled with advances in intelligent data processing, these developments are transforming laser interferometry into a versatile platform for comprehensive, multi-scale, and multi-parameter investigation of electrochemical systems. This progress will further deepen the mechanistic understanding of interfacial phenomena and provide valuable tools for the optimization of next-generation electrochemical energy devices.

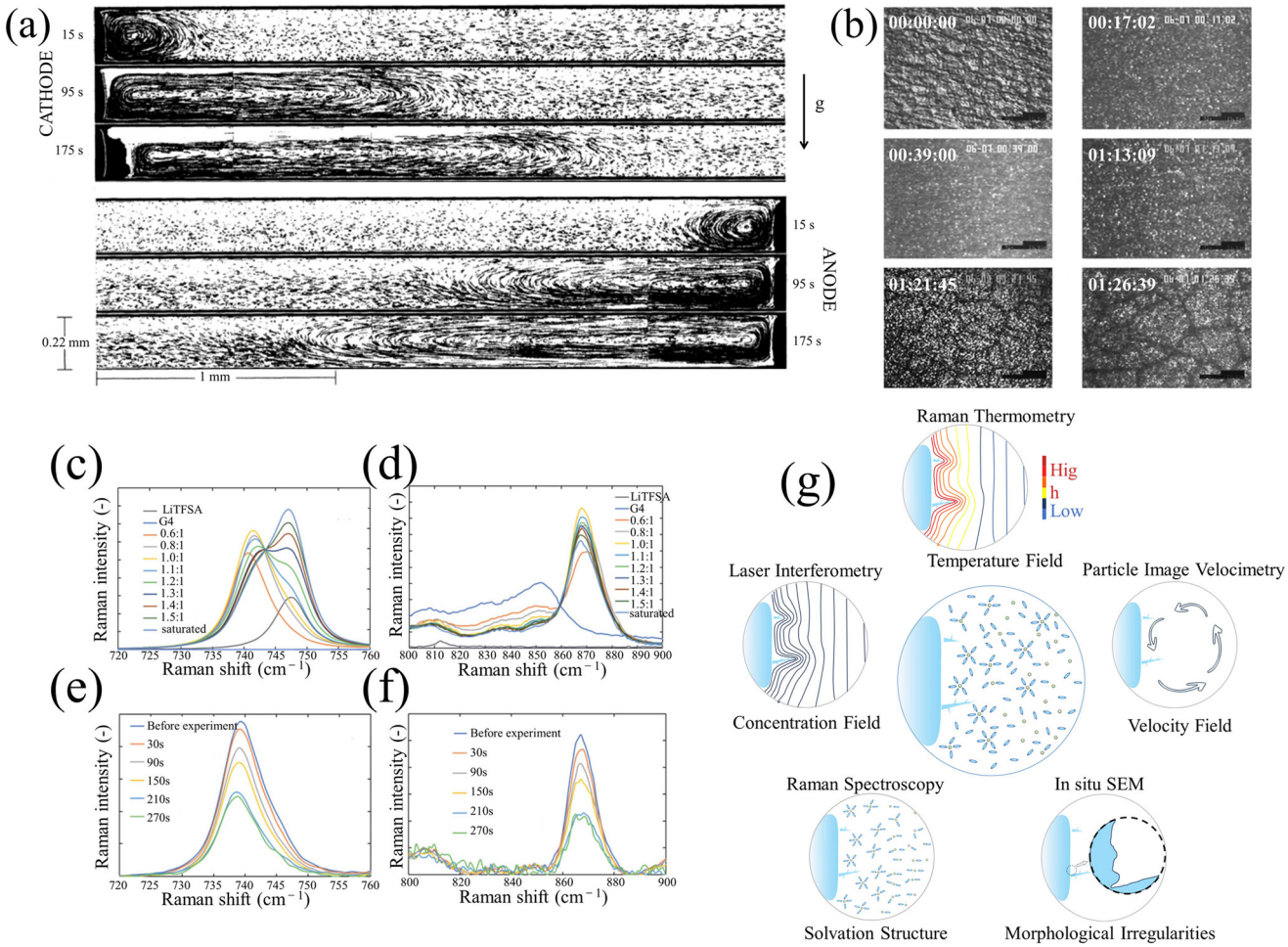

Fig. 10 Integrating laser interferometry with multimodal techniques. (a) Natural convection at the electrode–electrolyte interface visualized by particle tracking:[29] electrolyte depletion near the cathode induces upwards buoyancy-driven flow, forming a clockwise circulation pattern, whereas a denser electrolyte near the anode sinks and reinforces the flow. Reproduced from ref. 29. With permission from the American Physical Society, copyright. (b) Surface morphological evolution of Ni–Sn alloy electrodes at different lithiation stages captured by laser scanning confocal microscopy (LSCM).[112] Adapted from ref. 112 with permission from Elsevier, copyright. (c–f) Raman spectra of LiTFSA powder, pure G4, and their mixtures: (c and d) static spectra in the 720–760 cm^{-1} and 800–900 cm^{-1} ranges, while (e and f) *in situ* spectral evolution during Li plating near the cathode.[104] Reproduced from ref. 104 with permission from the Royal Society of Chemistry, copyright. (g) Schematic summary of various *in situ* techniques for probing electrode-electrolyte interfaces, with each module annotated by technique (top) and the corresponding parameter it resolves (bottom).

4. Conclusion

This work provides a comprehensive overview of laser interferometry as applied to electrochemical interface studies. Starting from fundamental optical principles and system configurations, interferogram-based concentration field reconstruction, quantitative data processing workflows, and the extraction of key transport parameters are systematically discussed. The representative applications are categorized based on characteristic interfacial behaviors, including concentration gradient evolution, metal deposition and dendrite growth, and convective mass transport. In addition to summarizing the technique's core strengths, such as high spatial–temporal resolution, non-invasiveness, and full-field imaging capability, this review also critically examines practical challenges encountered in electrochemical environments, including thickness-averaging effects, limited species specificity, and sensitivity to flow and temperature-induced artifacts.

By establishing a comprehensive methodological framework, this work provides valuable guidance for researchers seeking to apply laser interferometry in the study of interfacial mass transport across a wide range of electrochemical systems. The insights presented here are expected to support both fundamental investigations and practical optimization of advanced energy storage devices. Furthermore, this review contributes to the development of data-driven models and promotes a deeper understanding of the cross-scale correlations between the interfacial structure and ion transport behavior.

In the future, further advances in this field will rely on overcoming persistent challenges such as three-dimensional field reconstruction, species-level resolution, and the decoupling of multiphysical effects. Multimodal integration strategies,

including multi-angle interferometry,[114–117] absorption imaging,[118–120] fluorescence tracing, and nanoscale probing,[121–128] when combined with intelligent data processing approaches such as deep learning and generative adversarial network (GAN)-based methods,[129,130] hold great promise for extending the capabilities of interferometric techniques. These developments are expected to further enhance the mechanistic understanding of interfacial processes and accelerate the rational design of next-generation electrochemical energy technologies.

Conflicts of interest

There are no conflicts to declare.

Data availability

No primary research results, software or code have been included and no new data were generated or analysed as part of this work.

Acknowledgements

Z. Zhao thanks the funding support from the National Natural Science Foundation of China (523B2061) and P. Tan acknowledges the financial support from the National Innovative Talents Program (GG2090007001).

References

1 Y. Li, H. Liu, J. Zang and W. Wang, *ACS Appl. Mater. Interfaces*, 2024, **16**, 4818–4826.
2 P. H. Notten and D. L. Danilov, *Adv. Chem. Eng. Sci.*, 2014, **4**, 62–72.
3 A. A. Wong, S. M. Rubinstein and M. J. Aziz, *Cell Rep. Phys. Sci.*, 2021, **2**, 100388.
4 Q. Cheng, L. Wei, Z. Liu, N. Ni, Z. Sang, B. Zhu, W. Xu, M. Chen, Y. Miao and L.-Q. Chen, *Nat. Commun.*, 2018, **9**, 2942.
5 J. Fawdon, J. Ihli, F. L. Mantia and M. Pasta, *Nat. Commun.*, 2021, **12**, 4053.
6 X. Lu, C. Zhu, Z. Wu, J. Xuan, J. S. Francisco and H. Wang, *J. Am. Chem. Soc.*, 2020, **142**, 15438–15444.
7 T. Yamanaka, H. Nakagawa, S. Tsubouchi, Y. Domi, T. Doi, T. Abe and Z. Ogumi, *ChemSusChem*, 2017, **10**, 855–861.
8 T. Yamanaka, H. Nakagawa, S. Tsubouchi, Y. Domi, T. Doi, T. Abe and Z. Ogumi, *Electrochim. Acta*, 2017, **234**, 93–98.
9 H. J. Chang, A. J. Ilott, N. M. Trease, M. Mohammadi, A. Jerschow and C. P. Grey, *J. Am. Chem. Soc.*, 2015, **137**, 15209–15216.
10 S. A. Krachkovskiy, J. D. Bazak, P. Werhun, B. J. Balcom, I. C. Halalay and G. R. Goward, *J. Am. Chem. Soc.*, 2016, **138**, 7992–7999.
11 S. A. Krachkovskiy, A. D. Pauric, I. C. Halalay and G. R. Goward, *J. Phys. Chem. Lett.*, 2013, **4**, 3940–3944.
12 M. Klett, M. Giesecke, A. Nyman, F. Hallberg, R. W. Lindström, G. R. Lindbergh and I. Furó, *J. Am. Chem. Soc.*, 2012, **134**, 14654–14657.
13 K. Coke, M. J. Johnson, J. B. Robinson, A. J. Rettie, T. S. Miller and P. R. Shearing, *ACS Appl. Mater. Interfaces*, 2024, **16**, 20329–20340.
14 Y. Chen, X. Li, J. Lian, K. Fu, Z. Zhao, Y. He and P. Tan, *ACS Appl. Mater. Interfaces*, 2024, **16**, 42321–42331.
15 N. A. Padilla, M. T. Rea, M. Foy, S. P. Upadhyay, K. A. Desrochers, T. Derus, K. A. Knapper, N. H. Hunter, S. Wood and D. A. Hinton, *ACS Sens.*, 2017, **2**, 903–908.
16 Y. Qiao, Z. Zhou, Z. Chen, S. Du, Q. Cheng, H. Zhai, N. J. Fritz, Q. Du and Y. Yang, *Nano Energy*, 2018, **45**, 68–74.
17 Y. Takahashi, D. Takamatsu, Y. Korchev and T. Fukuma, *JACS Au*, 2023, **3**, 1089–1099.
18 T. Tahara, X. Quan, R. Otani, Y. Takaki and O. Matoba, *Microscopy*, 2018, **67**, 55–67.
19 A. Jahanbakhsh, K. L. Wlodarczyk, D. P. Hand, R. R. Maier and M. M. Maroto-Valer, *Sensors*, 2020, **20**, 4030.
20 B. Yogurtcu, N. Cebi, A. T. Koçer and A. Erarslan, *Molecules*, 2024, **29**, 5324.
21 A. D. Elliott, *Curr. Protoc. Cytom.*, 2020, **92**, e68.
22 X. Xu, D. Valavanis, P. Ciocci, S. Confederat, F. Marcuccio, J.-F. Lemineur, P. Actis, F. Kanoufi and P. R. Unwin, *Anal. Chem.*, 2023, **95**, 319–356.
23 C. Knox, R. R. Sayano, E. T. Seo and H. P. Silverman, *J. Phys. Chem.*, 1967, **71**, 3102–3104.
24 R. O'Brien and K. Santhanam, *Electrochim. Acta*, 1987, **32**, 1679–1691.
25 R. O'Brien and K. Santhanam, *J. Electrochem. Soc.*, 1982, **129**, 1266.
26 J. Newman and T. W. Chapman, *AIChE J.*, 1973, **19**, 343–348.
27 F. McLarnon, R. Muller and C. Tobias, *Electrochim. Acta*, 1976, **21**, 101–105.
28 D. Barkey, D. Watt, Z. Liu and S. Raber, *J. Electrochem. Soc.*, 1994, **141**, 1206.
29 J. M. Huth, H. L. Swinney, W. D. McCormick, A. Kuhn and F. Argoul, *Phys. Rev. E*, 1995, **51**, 3444.
30 F. Argoul, E. Freysz, A. Kuhn, C. Léger and L. Potin, *Phys. Rev. E*, 1996, **53**, 1777.
31 C. Léger, J. Elezgaray and F. Argoul, *Phys. Rev. E*, 1998, **58**, 7700.
32 H. You, J. Fang, F. Chen, C. Zhu, X. Song and B. Ding, *Chem. Phys. Lett.*, 2008, **465**, 131–135.
33 D. Ambrosini, D. Paoletti and N. Rashidnia, *Opt. Lasers Eng.*, 2008, **46**, 852–864.
34 C. Wang, S. Chen, X. Yang and L. Li, *Electrochem. Commun.*, 2004, **6**, 1009–1015.
35 X. Yang, S. Chen, C. Wang and L. Li, *Electrochem. Commun.*, 2004, **6**, 643–647.
36 B. Yuan, C. Wang, L. Li and S. Chen, *Electrochem. Commun.*, 2009, **11**, 1373–1376.
37 B. Yuan, S. Chen, X. Yang, C. Wang and L. Li, *Electrochem. Commun.*, 2008, **10**, 392–396.
38 C. Lai, B. Yuan, H. Dai, K. Xi, C. J. Harris, C. Wang and R. V. Kumar, *J. Phys. Chem. C*, 2017, **121**, 24733–24739.
39 H. Dai, B. Yuan, C. Bai, C. Lai and C. Wang, *J. Electrochem. Soc.*, 2018, **165**, A2866.

40 M. Li, K. Xie, R. Peng, B. Yuan, Q. Wang and C. Wang, *Small*, 2022, **18**, 2107398.
41 X. Xu, M. Song, M. Li, Y. Xu, L. Sun, L. Shi, Y. Su, C. Lai and C. Wang, *Chem. Eng. J.*, 2023, **454**, 140364.
42 G. Kamesui, K. Nishikawa, M. Ueda and H. Matsushima, *ACS Energy Lett.*, 2022, **7**, 4089–4097.
43 J. Colombani and J. Bert, *J. Mol. Liq.*, 2007, **134**, 8–14.
44 C. Guerrero-Mendez, T. Saucedo-Anaya, M. Araiza-Esquivel, E. De la Rosa and C. Olvera-Olvera, *Emerging Challenges for Experimental Mechanics in Energy and Environmental Applications*, Springer International Publishing, Cham, 2017.
45 M. He, S. Zhang, Y. Zhang and S. Peng, *Opt. Express*, 2015, **23**, 10884–10899.
46 C. Guerrero Méndez, T. Saucedo Anaya, M. A. Araiza Esquivel, R. E. Balderas Navarro, A. López Martínez and C. A. Olvera Olvera, *Metrol. Meas. Syst.*, 2017, **24**, 19–26.
47 S. Zhang, M. He, Y. Zhang, S. Peng and X. He, *Appl. Opt.*, 2015, **54**, 9127–9135.
48 V. K. Chhaniwal, A. Anand, S. Girhe, D. V. Patil, N. Subrahmanyam and C. S. Narayanamurthy, *J. Opt. A:Pure Appl. Opt.*, 2003, **5**, S329–S337.
49 B. Hundhammer, S. K. Dhawan, A. Bekele and H. J. Seidlitz, *J. Electroanal. Chem. Interfacial Electrochem.*, 1987, **217**, 253–259.
50 C. Mattisson, D. Karlsson, S.-G. Pettersson, G. Zacchi and A. Axelsson, *J. Phys. D: Appl. Phys.*, 2001, **34**, 3088–3096.
51 D. Mayorga-Cruz, P. Márquez-Aguilar, O. Sarmiento-Martinez and J. Uruchurtu-Chavarín, *Opt. Lasers Eng.*, 2007, **45**, 140–144.
52 K. Habib, *Corros. Sci.*, 2001, **43**, 449–455.
53 K. Habib, *Opt. Lasers Eng.*, 1993, **18**, 115–120.
54 K. Nishikawa, E. Chassaing and M. Rosso, *Electrochim. Acta*, 2011, **56**, 5464–5471.
55 M. Born and E. Wolf, *Principles of Optics: Electromagnetic Theory of Propagation, Interference and Diffraction of Light*, Pergamon, Oxford, 2013.
56 G. Kamesui, K. Nishikawa, M. Ueda and H. Matsushima, *Electrochem. Commun.*, 2023, **151**, 107506.
57 J. M. Mehta and W. M. Worek, *Appl. Opt.*, 1984, **23**, 928–933.
58 D. Watt and C. Vest, *Exp. Fluids*, 1987, **5**, 401–406.
59 T. Colomb, E. Cuche, F. Charrière, J. Kühn, N. Aspert, F. Montfort, P. Marquet and C. Depeursinge, *Appl. Opt.*, 2006, **45**, 851–863.
60 U. Schnars and W. Jüptner, *Appl. Opt.*, 1994, **33**, 179–181.
61 V. Abbasian, E. A. Akhlaghi, M. A. Charsooghi, M. Bazzar and A.-R. Moradi, *Ultramicroscopy*, 2018, **185**, 72–80.
62 X.-J. Lai, Y.-C. Lin, H.-Y. Tu and C.-J. Cheng, *Sci. Rep.*, 2018, **8**, 5943.
63 V. G. Levich and C. W. Tobias, *J. Electrochem. Soc.*, 1963, **110**, 251C.
64 J. K. Novev and R. G. Compton, *Curr. Opin. Electrochem.*, 2018, **7**, 118–129.
65 B. Cai, J. Ge, F. Zhu, Y. Gao and S. Jiao, *J. Electroanal. Chem.*, 2023, **950**, 117865.
66 E. L. Cussler, *Diffusion: Mass Transfer in Fluid Systems*, Cambridge University Press, Cambridge, 2009.
67 D. R. Lide, *CRC Handbook of Chemistry and Physics: A Ready-Reference Book of Chemical and Physical Data*, CRC press, Boca Raton, FL, 1994.
68 C. Amatore, S. Szunerits, L. Thouin and J.-S. Warkocz, *J. Electroanal. Chem.*, 2001, **500**, 62–70.
69 T. Latychevskaia, *Appl. Opt.*, 2019, **58**, 3597–3603.
70 J. Garcia-Sucerquia, W. Xu, M. Jericho and H. J. Kreuzer, *Opt. Lett.*, 2006, **31**, 1211–1213.
71 F. R. Mclarnon, R. H. Muller and C. W. Tobias, *J. Electrochem. Soc.*, 1975, **122**, 59–64.
72 C. Vest, *Opt. Eng.*, 1980, **19**, 654–658.
73 F. McLarnon, R. Muller and C. Tobias, *Ind. Eng. Chem. Fundam.*, 1979, **18**, 97–108.
74 D. Naylor, *Int. J. Heat Fluid Flow*, 2003, **24**, 345–355.
75 J. Zhou, J. Shen and W. S. Neill, *Rev. Sci. Instrum.*, 2016, **87**, 073104.
76 M. M. El-Wakil and P. A. Ross, Liquid propellants and propulsion, in *Progress in Astronautics and Rocketry*, ed. L. E. Bollinger, M. Goldsmith and A. W. Lemmon Jr, Academic Press, New York, 1960, vol. 2, pp. 265–298.
77 W. Panknin, *Eine holographische Zweiwellenlängen-Interferometrie zur Messung überlagerter Temperatur- und Konzentrationsgrenzschichten*, Technische Universität Hannover, 1977.
78 F. Mayinger, in *Optical Measurements: Techniques and Applications*, ed. F. Mayinger and O. Feldmann, Springer, Berlin, Heidelberg, 2001.
79 S. Montresor and P. Picart, *Opt. Express*, 2016, **24**, 14322–14343.
80 F. Charrière, B. Rappaz, J. Kühn, T. Colomb, P. Marquet and C. Depeursinge, *Opt. Express*, 2007, **15**, 8818–8831.
81 Y. Surrel, *Appl. Opt.*, 1997, **36**, 271–276.
82 Y. Rivenson, Y. Zhang, H. Günaydın, D. Teng and A. Ozcan, *Light:Sci. Appl.*, 2018, **7**, 17141.
83 Y. Wu, Y. Rivenson, Y. Zhang, Z. Wei, H. Günaydin, X. Lin and A. Ozcan, *Optica*, 2018, **5**, 704–710.
84 Z. Ren, Z. Xu and E. Y. Lam, *Adv. Photonics*, 2019, **1**, 016004.
85 T. Zeng, Y. Zhu and E. Y. Lam, *Opt. Express*, 2021, **29**, 40572–40593.
86 I. M. Sakr, W. El-Askary, A. Balabel and K. Ibrahim, *CFD Lett.*, 2013, **5**, 81–96.
87 M. Ota, S. Izuo, K. Nishikawa, Y. Fukunaka, E. Kusaka, R. Ishii and J. Selman, *J. Electroanal. Chem.*, 2003, **559**, 175–183.
88 X. Yang, K. Eckert, A. Heinze and M. Uhlemann, *J. Electroanal. Chem.*, 2008, **613**, 97–107.
89 S. Kawai, K. Nishikawa, Y. Fukunaka and S. Kida, *Electrochim. Acta*, 2007, **53**, 257–264.
90 S. Kawai, Y. Fukunaka and S. Kida, *J. Electrochem. Soc.*, 2009, **156**, F99.
91 Y. Fukunaka, Y. Nakamura and Y. Konishi, *J. Electrochem. Soc.*, 1998, **145**, 3814.
92 Y. Awakura, Y. Takenaka and Y. Kondo, *Electrochim. Acta*, 1976, **21**, 789–797.

93 S. Kawai, Y. Fukunaka and S. Kida, *J. Electrochem. Soc.*, 2009, **156**, F109.
94 G. Nelissen, A. Van Theemsche, C. Dan, B. Van den Bossche and J. Deconinck, *J. Electroanal. Chem.*, 2004, **563**, 213–220.
95 K. Nishikawa, Y. Fukunaka, T. Sakka, Y. Ogata and J. Selman, *J. Electroanal. Chem.*, 2005, **584**, 63–69.
96 K. Nishikawa, Y. Fukunaka, T. Sakka, Y. Ogata and J. Selman, *J. Electrochem. Soc.*, 2007, **154**, A943.
97 W. Li, B. Yuan, C. Wang, L. Li and S. Chen, *Sensors*, 2012, **12**, 4962–4973.
98 B. Yuan, C. Wang, L. Li and S. Chen, *Russ. J. Electrochem.*, 2012, **48**, 804–809.
99 B. Yuan, W. Li, C. Wang and L. Li, *Sens. Actuators, B*, 2013, **176**, 509–513.
100 B. Yuan, S. Tong, X. Zhang, L. Li and C. Wang, *Measurement*, 2017, **98**, 10–16.
101 G. Kamesui, K. Nishikawa, M. Ueda and H. Matsushima, *J. Electrochem. Soc.*, 2024, **171**, 040519.
102 G. Kamesui, K. Nishikawa, M. Ueda and H. Matsushima, *Electrochem. Commun.*, 2023, **151**, 107506.
103 Y. Fukunaka, T. Yamamoto and Y. Kondo, *J. Electrochem. Soc.*, 1989, **136**, 3630.
104 A. Miki, K. Nishikawa, G. Kamesui, H. Matsushima, M. Ueda and M. Rosso, *J. Mater. Chem. A*, 2021, **9**, 14700–14709.
105 R. O'Brien and K. Santhanam, *J. Appl. Electrochem.*, 1990, **20**, 427–437.
106 C. Wang, S. Chen and X. Yu, *Electrochim. Acta*, 1994, **39**, 577–580.
107 C. Wang and S. Chen, *Electrochim. Acta*, 1998, **43**, 2225–2232.
108 C. Wang and S. Chen, *J. Serb. Chem. Soc.*, 2001, **66**, 477–481.
109 B. Yuan, C. Wang, L. Li and S. Chen, *Corros. Sci.*, 2012, **58**, 69–78.
110 S. Liu, Y. Shao, C. Yan, B. Yuan, L. Li and C. Wang, *Corros. Sci.*, 2020, **169**, 108614.
111 K. Nishikawa, M. Ota, S. Izuo, Y. Fukunaka, E. Kusaka, R. Ishii and J. Selman, *J. Solid State Electrochem.*, 2004, **8**, 174–181.
112 K. Nishikawa, Y. Fukunaka, T. Sakka, Y. Ogata and J. R. Selman, *J. Power Sources*, 2007, **174**, 668–672.
113 E. Tada and H. Kaneko, *Corros. Sci.*, 2010, **52**, 3421–3427.
114 A. Srivastava, K. Tsukamoto, E. Yokoyama, K. Murayama and M. Fukuyama, *J. Cryst. Growth*, 2010, **312**, 2254–2262.
115 S. Sugawara, S. Nakao, Y. Miyazato, Y. Ishino and K. Miki, *J. Fluid Mech.*, 2020, **893**, A25.
116 A. Klee, S. T. Thurman and T. Alley, *Unconventional Imaging and Adaptive Optics 2021*, SPIE, Bellingham, WA, 2021.
117 P. Psota, M. Stašík, M. Jiránek, V. Lédl and J. Hála, *Opt. Lasers Eng.*, 2025, **184**, 108566.
118 N. Pavillon, A. Benke, D. Boss, C. Moratal, J. Kühn, P. Jourdain, C. Depeursinge, P. J. Magistretti and P. Marquet, *J. Biophotonics*, 2010, **3**, 432–436.
119 Y. N. Nygate, G. Singh, I. Barnea and N. T. Shaked, *Opt. Lett.*, 2018, **43**, 2587–2590.
120 N. Pande, S. K. Chandrasekar, D. Lohse, G. Mul, J. A. Wood, B. T. Mei and D. Krug, *J. Phys. Chem. Lett.*, 2020, **11**, 7042–7048.
121 S.-J. Lee and S. Kim, *Meas. Sci. Technol.*, 2004, **15**, 664.
122 B. Figueroa, R. Hu, S. G. Rayner, Y. Zheng and D. Fu, *J. Phys. Chem. Lett.*, 2020, **11**, 7083–7089.
123 X. Lu, Y. Chen, F. Mazza, S. He, Z. Li, S. Huang, Q. Wang, N. Zhang, B. Shen and Y. Wu, *Light:Sci. Appl.*, 2024, **13**, 315.
124 J. F. Torres, Y. Zhao, S. Xu, Z. Li and A. Komiya, *Phys. Rev. Appl.*, 2020, **14**, 054038.
125 L. F. Olbrich, B. Jagger, J. Ihli and M. Pasta, *ACS Energy Lett.*, 2024, **9**, 3636–3642.
126 D. Perry, A. Page, B. Chen, B. G. Frenguelli and P. R. Unwin, *Anal. Chem.*, 2017, **89**, 12458–12465.
127 S. M. Leitao, B. Drake, K. Pinjusic, X. Pierrat, V. Navikas, A. P. Nievergelt, C. Brillard, D. Djekic, A. Radenovic and A. Persat, *ACS Nano*, 2021, **15**, 17613–17622.
128 G. Rong, X. Zhang, W. Zhao, Y. Qiu, M. Liu, F. Ye, Y. Xu, J. Chen, Y. Hou and W. Li, *Adv. Mater.*, 2017, **29**, 1606187.
129 T. Shimobaba, D. Blinder, T. Birnbaum, I. Hoshi, H. Shiomi, P. Schelkens and T. Ito, *Front. Photonics*, 2022, **3**, 854391.
130 Q. Fang, H. Xia, Q. Song, M. Zhang, R. Guo, S. Montresor and P. Picart, *Opt. Express*, 2022, **30**, 20666–20683.